

POLYTECHNIC UNIVERSITY OF TURIN

Master's Degree in Mechatronic Engineering:
Technologies for E-mobility



Master's Degree Thesis

Implementation of Virtual Point Transformation and Modal analysis for automotive Rim and Hub

Thesis supervisors:

Prof. Stefano Alberto MALAN

Engineer Domenico MINERVINI

Student:

Riccardo COPPINI

December 2023

Summary

The aim of this thesis project is to test and validate through simulation the NVH performances for an automotive component. The automotive component considered is an automotive rim. During the project is also reported a simulation of different kind of coupling between the automotive rim and a model of an hub designed on the software Simcenter 3D. The method leveraged during the analysis is the Virtual Point Transformation method (VPT): a theoretical method leveraged in CAE. This kind of method allow to retrieve the frequency response function of a virtual point starting from real measurements gathered in a testing environment. Firstly, a general overview of the NVH field, its purposes, challenges and current industrial problems related to it is given. Then the theoretical background needed to appreciate the problems illustrated, considering the FEA, the Modal analysis and an illustration of the virtual point transformation method are depicted. To retrieve the frequency response functions through simulation and to evaluate the scenarios studied the modal analysis, the real eigenvalue analysis and direct frequency response analysis are leveraged. Their knowledge is required to implement the different solvers used on the software Simcenter Nastran and Simcenter 3D. A validation of the followed analysis is applied on structures from one to three dimensions, considering a solid beam, a plate and the automotive rim. One of the purposes of this thesis is to represent through simulation experimental issues of the VPT method applied in CAE, considering problems that are still to be optimized and under study. The project conclude with a study conducted considering the coupling between the automotive rim and the hub, in order to investigate the influence of the flexibility on the accuracy of the virtual point transformation method.

Acknowledgements

Con questa tesi si chiude un capitolo della mia vita che ha significato molto per me e la mia crescita personale. Sono contento di aver intrapreso questo percorso che mi ha portato ad avvicinarmi a diventare la persona o il modello che un giorno vorrei raggiungere. Credo che ognuno di noi in questo percorso che è la vita, sia alla costante ricerca di diventare una persona migliore. Una persona più buona, che possa essere di aiuto alle persone più care e che possa contribuire a migliorare la società in cui viviamo. In questo viaggio oggi posso mettere un paletto, in cui posso fermarmi, voltarmi, salutare il Riccardo del passato e magari ispirarlo. Sono stati anni in cui ho avuto la fortuna di vivere un ampio spettro di emozioni e un altalena di esperienze.

Vorrei ringraziare i miei genitori dai quali ho sempre avuto supporto, nonostante le tante preoccupazioni che gli ho potuto dare mi sono sempre stati vicino accettando qualsiasi scelta io abbia preso e supportandomi. Grazie a mio padre che mi ha insegnato a sognare e a coltivare l'immaginazione. Grazie a mia madre per aver sempre creduto in me, per avermi ispirato nell'uscire da ogni situazione avendo fede nel futuro. Vorrei ringraziare mia sorella Marta per la quale ho un'infinita stima, sono grato e fortunato per aver avuto questo dono, lei che posso considerare la mia supereroina. Mi è sempre stata accanto in questi anni nei momenti belli ma specialmente nei momenti più duri, dove volevo gettare la spugna, lei che è sempre riuscita a destreggiarsi tra mille difficoltà. Mi ha insegnato a sorridere in qualsiasi situazione e di fronte a qualsiasi ostacolo. Vorrei ringraziare mia nonna Maria la quale non è più tra noi e che spero di aver reso orgogliosa. Per me è stata una madre che mi ha sempre incitato e sempre spinto a vedere la bellezza nel mondo e nella vita. Ringrazio mia nonna Ida per avermi insegnato a non prendermi sul serio e ad affrontare le delusioni e i momenti difficili con allegria. Ringrazio mio zio Vito per avermi sempre sostenuto ed avermi insegnato valori fondamentali come la disciplina, il lavoro ed il rispetto senza i quali non avrei potuto raggiungere niente. Ringrazio Michele, per me un'ancora di salvezza durante questi anni, una delle persone più belle e con il cuore più puro che abbia mai conosciuto, che mi ha sempre fatto vedere il bicchiere mezzo pieno in ogni situazione. Assieme a Michele ringrazio anche Giulio per le divertenti escursioni passate insieme. Ringrazio Alberto per essere sempre

stato al mio fianco in questi anni risolvendola sempre con una partita a tennis o un film al cinema, strappandomi sempre un sorriso anche nei momenti più duri. Vorrei ringraziare tutti i miei cugini e tutti i miei affetti in Puglia, tra cui Paolo, Marco e Filippo, con cui sono cresciuto. Mi hanno sempre risollevato e spinto a credere in me stesso, sono fiero di loro e per i successi che hanno raggiunto e raggiungeranno. Ringrazio Luigi, una delle persone più straordinarie che abbia mai conosciuto, per me è stato un mentore, un modello di ispirazione. Lo ringrazio per avermi dato la voglia di sognare, di credere in me stesso e non accontentarmi, di accogliere a braccia aperte ogni sfida e di esplorare nuove nazioni e culture. Ringrazio anche gli amici che ho conosciuto in Belgio, tra cui Maurizio, Piero, Michele e Josh che posso considerare come fratelli e insieme ai quali ho vissuto esperienze indimenticabili. Ringrazio Giuliano per avermi insegnato l'arte della pesca, a conoscere la pazienza, a reinventarmi sempre in ogni situazione e vedere la vita come un'avventura da riempire di esperienze. Ringrazio Adalberto e Giuseppina per il loro caldo supporto durante questi anni. Ringrazio Ettore, Daniela e Serafico per le belle serate d'estate tra un esame e l'altro. Ringrazio Mattia, sebbene sia entrato da poco in famiglia si è dimostrato un amico che ti colora le giornate e sa quanto prendere la vita con leggerezza. Ringrazio i miei amici conosciuti a Torino tra cui Sebastiano ed Adelaide, con cui abbiamo affrontato ogni esame supportandoci e dandoci forza a vicenda. Ringrazio infine mia zia Mirella, una delle persone più generose e con l'animo più gentile che possano esistere. Sono grato per ogni persona che ho incontrato nel mio cammino e la serie di esperienze che ho vissuto, di cui so che questo traguardo ne segna solo l'inizio.

This thesis closes a chapter in my life that has represented a great step forward for me and my personal growth. I am glad that I have undertook this path that has brought me closer to becoming the person or role model that I would like to achieve one day. I genuinely believe that each one of us in this journey called life can find himself in a constant search to become a better human being. A person careful to become more kind, more helpful to the people that he cares and that can contribute and bring value to the society in which we live. On this point of this journey, today I can put a stake, on which I can stop, turn back, greet the younger Riccardo of the past and hopefully inspire him. These had been years for which I consider myself lucky to have lived, years in which I had the opportunity to live a wide spectrum of emotions and a rollercoaster of experiences. I would like to thank my parents from which I always had support, even though the various worries that I could have gave them, they always remained close to me and accepted each choice that I have made. I would like to thank my father Bruno that taught me to dream and nurture my imagination. I would like to thank my mother Margherita for having always believed in me, for having inspired me to come out from every situation keeping faith in the future. I would like to thank my sister Marta for whom I have infinite esteem, I feel grateful and lucky for this gift. She always has been by my side during these years both in the good and especially in the hard times, where I would have wanted to quit, she that always accomplished to succeed among various difficulties. She taught me to laugh in front of every situation and obstacle. I would like to thank my grandmother Maria that is not anymore among us and that I hope I have made proud. For me she has been a mother that always urged me to see the beauty in the world and in life. I would like to thank my grandmother Ida for having me taught to don't take myself seriously and confront the delusions and hard times with cheerfulness. I would like to thank my uncle Vito for having always supported me and having me taught extremely important values such as discipline, work attitude and respect without which I wouldn't have accomplished nothing. I would like to thank Michele, for me an anchor during these years, one of the most kind persons and with the purest heart that I have ever met, that made me always see positively each moment. Together with him I would like to thank Giulio for the free time spent hiking and the funny activities in the wild. I would like to thank Alberto that has always been by my side during these years, having fun playing tennis or spending evenings at the cinema, wringing a laugh out of me in the hardest periods. I would like to thank all my cousins and bondings in Puglia, among them in particular Paolo, Marco and Filippo, with which I grew up. They always lifted me up e pushed me to having faith in myself, I am proud of them and the achievements that they have reached and will reach. I would like to thank Luigi, one of the most extraordinary persons that I have ever met: he has been a mentor for me, a inspirational model. I thank him for giving me the will to dream, to believe in myself, to always be hungry and accept every challenge

and explore different countries and cultures. I would like to thank my friends that I have met in Belgium, among which Maurizio, Piero, Michele and Josh which I can consider as brothers to me and with which I had the opportunity to live unforgettable experiences. I would like to thank Giuliano for having taught me the art of fishing, to learn the patience, to always reinvent myself in each situation and to see life as an adventure to fill with experiences. I would like to thank Adalberto and Giuseppina for their warm support during these years. I would like to thank Ettore, Daniela and Serafico for the beautiful evenings during the summers spent between the university exams. I would like to thank Mattia, even if he entered in our family from a small amount of time he became a friend that can colour your days and who knows how to take life with lightness. I would like to thank my friends met in Turin especially Sebastiano and Adelaide, with which we overcame every exams supporting and giving strenght to each other. I would like to thank my aunt Mirella, one of the persons with the most generous purest heart that can exist. I am truly grateful for every person that I have met in this path and the series of experience that I have lived, of which I know that this achievement represent only the beginning.

Table of Contents

| | |
|--|----|
| List of Tables | X |
| List of Figures | XI |
| Acronyms | XV |
| 1 Introduction | 1 |
| 1.1 What is NVH | 1 |
| 1.1.1 Applications and cases of study | 3 |
| 1.2 Why do we study Dynamic Substructuring | 6 |
| 1.3 Current industrial problems | 8 |
| 2 Theoretical Background | 12 |
| 2.1 Finite Element Analysis | 12 |
| 2.1.1 Formulation | 14 |
| 2.2 Modal analysis | 18 |
| 2.2.1 Formulation | 18 |
| 2.2.2 Modal frequency response | 20 |
| 2.3 Virtual Point Transformation | 23 |
| 2.3.1 Formulation using translation | 24 |
| 2.3.2 Formulation using translation and rotation | 28 |
| 3 Applications of Modal analysis and VPT | 32 |
| 3.1 Modal analysis of a cantilever beam | 33 |
| 3.1.1 Dynamic analysis of a cantilever beam SOL 103 | 33 |
| 3.1.2 Modal frequency response analysis: cantilever beam SOL 111 | 35 |
| 3.1.3 Direct frequency response analysis of a cantilever beam (load at the end) SOL 108 | 36 |
| 3.2 VPT application | 37 |
| 3.2.1 Square plate | 37 |
| 3.2.2 Automotive Rim | 40 |

| | | |
|----------|--|-----------|
| 4 | Experimental Issues of VPT in CAE | 45 |
| 4.1 | Experimental issues in real testing environment | 45 |
| 4.2 | Sensitivity analysis | 47 |
| 4.2.1 | Rigid connection VP-center hole/VP-indicators and comparison | 47 |
| 4.2.2 | Influence of the distance of the indicators on the accuracy of VPT | 53 |
| 4.3 | Environmental Error analysis | 57 |
| 4.3.1 | Output moved radially along the Rim | 57 |
| 4.3.2 | Output moved around the input - Close and Far distances . | 60 |
| 4.3.3 | Reproduction of Indicators as sensors and validation of reci- procity | 64 |
| 5 | Modal analysis for Coupled Interfaces | 71 |
| 5.1 | Glued connection | 73 |
| 5.2 | Single rigid connection | 74 |
| 5.3 | Multiple rigid connection | 75 |
| 5.4 | Comparison & analysis | 76 |
| 6 | Conclusions and further improvements | 83 |
| | Bibliography | 85 |

List of Tables

| | | |
|-----|---|----|
| 3.1 | Indicators and VP coordinates of the square plate case. | 38 |
| 3.2 | Indicators and VP coordinates of the automotive rim case. | 42 |
| 5.1 | Number of modes showed under $8000Hz$ | 76 |

List of Figures

| | | |
|------|--|----|
| 1.1 | Noise from an automotive vehicle.[1] | 2 |
| 1.2 | Automotive driveline, source of noise and vibrations [5]. | 3 |
| 1.3 | Vibrations from the tire to the cabin [6]. | 3 |
| 1.4 | Teardrop accelerometer. [8] | 4 |
| 1.5 | Capacitive microphone [10]. | 5 |
| 1.6 | Miniature shaker for automotive NVH testing [11]. | 5 |
| 1.7 | Domains of Dynamic Substructuring [13]. | 7 |
| 1.8 | Electric motor & transmission [17]. | 9 |
| 1.9 | The propulsion noise, the tyre/road noise and the total noise from a passenger car calculated with the Nord2000 noise prediction model [18]. | 10 |
| 1.10 | Noise level comparison between EV and ICE vehicles at various speeds [19]. | 11 |
| 2.1 | Finite Element Analysis applications. | 13 |
| 2.2 | Process of FEM. | 15 |
| 2.3 | Definition of the regions in the geometry. | 15 |
| 2.4 | FEM from continuous to set of unknowns. | 17 |
| 2.5 | Decomposition in modes of the structure of the dynamic behavior. | 19 |
| 2.6 | Schematic representation of the substructuring problem. | 24 |
| 2.7 | Example of interface connection with VP and triaxial translation sensor. | 26 |
| 2.8 | Case of a cantilever beam with two translation sensors placed on the free end. | 29 |
| 2.9 | Effect of calibration error in the sensor sensitivity: a) translational FRF Y_{u_2} ; b) rotational FRF Y_θ [32]. | 29 |
| 2.10 | Example of the interface with virtual point and a triaxial rotational sensor. | 30 |
| 3.1 | Cantilever beam, real eigenvalue analysis: Matlab plot mode 2, 5 and 9. | 34 |

| | | |
|------|---|----|
| 3.2 | Cantilever beam, real eigenvalue analysis: animation of mode 2, 5 and 9 on Simcenter 3D. | 35 |
| 3.3 | Cantilever beam, modal frequency response analysis: FRF from 0Hz to 2048Hz. | 36 |
| 3.4 | Cantilever beam, comparison SOL108 & SOL111 until 3000Hz. | 37 |
| 3.5 | Square plate model on Simcenter 3D. | 39 |
| 3.6 | Comparison plot of the response of the virtual point along the x-axis. | 40 |
| 3.7 | 3D model of the BMW 128 rim. | 41 |
| 3.8 | Tetrahedral mesh of the BMW 128 rim. | 42 |
| 3.9 | Response of the automotive rim with direct and response applying vpt, F_y as input and a_x as output. | 43 |
| 4.1 | NVH test on an automotive rim: location of the indicators. | 46 |
| 4.2 | Area of connection of the automotive rim: VP-Indicators. | 48 |
| 4.3 | RBE2 connections between the virtual point and the indicators. | 48 |
| 4.4 | Plot of the linear response of the case with hypothesis of rigidity. | 49 |
| 4.5 | Area of connection of the automotive rim: VP-Center hole. | 50 |
| 4.6 | Back side of the rim, plane of the RBE2 connections and the virtual point. | 50 |
| 4.7 | Plot of the linear response of the case without hypothesis of rigidity. | 51 |
| 4.8 | Virtual point transformation: no rigidity hypothesis. | 51 |
| 4.9 | Positioning of the indicators in two distances. | 53 |
| 4.10 | Response comparing reference, close and far indicators. Input F_x and output a_x | 54 |
| 4.11 | Mode shape 8 at 535Hz | 55 |
| 4.12 | Animation of the eight mode shape | 55 |
| 4.13 | Mode shapes 11, 12 & 13 | 56 |
| 4.14 | Mode shapes 11, 12 & 13 | 56 |
| 4.15 | Case: indicators moved along the radius of the automotive rim. | 57 |
| 4.16 | Response along $z - axis$ with linear input and output. | 59 |
| 4.17 | FRF linear responses and output: Loss of the symmetry. | 60 |
| 4.18 | Distribution of the input output locations of five set of nodes, close to the virtual point. | 61 |
| 4.19 | Response on F_y as input and a_y as output. | 62 |
| 4.20 | Distribution of the input and output locations of five set of nodes, far from the virtual point. | 63 |
| 4.21 | Response with input F_y and output a_y | 64 |
| 4.22 | Indicators location and structure. | 65 |
| 4.23 | RBE2 distribution: on the left the connections with the virtual point (VP), on the right that ones representing the indicators. | 66 |

| | | |
|------|--|----|
| 4.24 | First case reproducing sensors, output in the surface of contact and input on top. | 67 |
| 4.25 | First case plot of the responses considering only linear inputs and outputs. | 68 |
| 4.26 | Second case reproducing sensors, input in the surface of contact and output on top. | 69 |
| 4.27 | Comparison between the responses of the first and second case. . . . | 70 |
| 5.1 | 3D model of the automotive rim and hub coupled. | 71 |
| 5.2 | 3D model of the automotive hub. | 72 |
| 5.3 | Focus on the connection on the " <i>Glued connection</i> " case. | 73 |
| 5.4 | Focus on the connection on the " <i>Single rigid connection</i> " case. . . . | 74 |
| 5.5 | Focus on the connection on the " <i>Multiple rigid connection</i> " case. . . | 75 |
| 5.6 | Comparison of the response with input F_y and output a_y : range of frequencies $0Hz - 4000Hz$ | 77 |
| 5.7 | Mode 11 response with input F_y and output a_y | 77 |
| 5.8 | Mode 11 response with input F_y and output a_y , animations on Simcenter 3D. | 78 |
| 5.9 | Comparison of the response with input F_z and output a_z : range of frequencies $0Hz - 2500Hz$ | 79 |
| 5.10 | Significant modes, response with input F_z and output a_z | 80 |
| 5.11 | Modes 14 – <i>th</i> and 15 – <i>th</i> for the single rigid connection, input load F_z | 80 |
| 5.12 | Mode 18 – <i>th</i> for the multiple and glued connections, input load F_z . . | 81 |

Acronyms

NVH

noise vibration harshness

HVAC

heat, ventilation and air conditioning

PCB

printed circuit board

PLM

product lifecycle management

FRF

frequency response function

EMA

experimental modal analysis

TPA

transfer path analysis

FBS

frequency based substructuring

CAE

computer aided engineering

C-TPA

component transfer path analysis

NEV

new energy vehicle

ICE

internal combustion engine

SPL

sound pressure level

BEV

battery electric vehicle

FEA

finite element analysis

FEM

finite element method

BC

boundary conditions

DISW

digital industries software

DOF

degree of freedom

LM FBS

lagrange multiplier frequency based substructuring

IDM

interface deformation mode

VPT

virtual point transformation

VP

virtual point

Chapter 1

Introduction



**POLITECNICO
DI TORINO**

In this chapter there is an overall introduction to the concepts and problems about Noise and Vibration Harshness (NVH), Dynamic Substructuring and current industrial problems that involves this two areas of study. There are also explained some challenges that still have to be handled, for instance the advent of the electrification of the vehicles for the NVH and improvements that are still ongoing in FBS.

1.1 Noise and vibrations in Automotive

Noise, Vibration and Harshness (NVH), also referred to as Noise and Vibration (N&V), is the study and adjustment of noise and vibration characteristics of a physical structure: it can interest every object that can vibrate and has an indirect or either direct human interaction as vehicles, washing machines, wind turbines for instance. The vehicles interested could be among the automotive field, marine field

and aerospace field. Namely this area of study can be applied from cars to ships as well as airplanes. In figure 1.1 it is shown an overview of the noise transmission on the external environment [1].



Figure 1.1: Noise from an automotive vehicle.[1]

The NVH field requires mainly knowledges from mechanical, aerospace, acoustic and electronic engineering [2], so the figure that can manage problems ensuing from it has to have a wide, even if general, perception of the topics involved. While structural dynamics is primarily studied in the mechanical domain, sensors and signal processing necessitate knowledge of electronic engineering. Here is showed an overview of the three phenomena considered:

- Noise: Sound generated from the intensity and the frequency of the vibrations of the vehicle. The acoustic noise is energy transmitted to the air that causes an audible disturbance.
- Vibration: Is an oscillation that causes noise and disturbance. The vibrations are transmitted between the components of the vehicle and among the interaction of the vehicle and the environment.
- Harshness: Is the only parameter that can be described entirely as a subjective quality, indeed to evaluate the harshness it can be subject to jury evaluations, or evaluated with electroacoustic equipment, in order to reflect human subjective impressions. It is generally used to describe the severity and discomfort associated with both vibration and noise.

The performances of a vehicle concerning noise, vibration and harshness as parameters have significant influence on the vehicle design and validation criteria. The main purpose of this study is for enhance the performances of the vehicle in terms of comfort and to predict possible mechanical damages of the components.

1.1.1 Applications and cases of study

The NVH on an automotive vehicle can ensue from different causes, as Wang Xu analyzed [3], namely from the HVAC (“Heating, Ventilation and Air Conditioning” [4]), so Aerodynamic nature; it could be also from mechanical sources, for instance from the engine, driveline (figure 1.2, [5]), tire contact patch and road surface as well as brakes. In figure 1.3 [6] it is shown the transmission of the vibrations from the tire to the cabin.

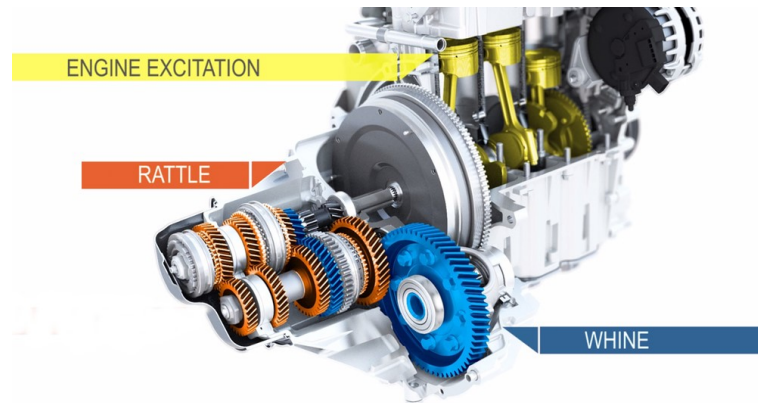


Figure 1.2: Automotive driveline, source of noise and vibrations [5].

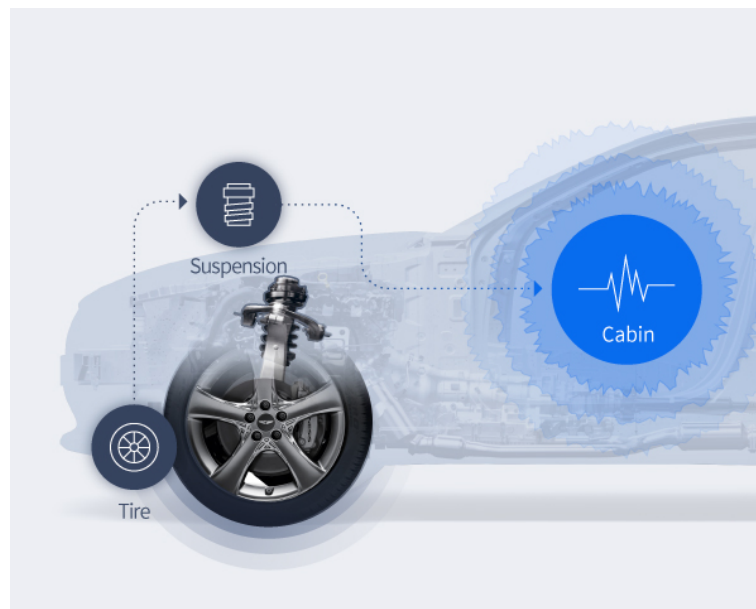


Figure 1.3: Vibrations from the tire to the cabin [6].

There are several tools leveraged for the NVH testing [7]:

- Accelerometer:

The accelerometer is a sensor that can measure the proper acceleration of an object. It is an electromechanical transducer that produces at its output terminals an electrical output proportional to the acceleration to which it is subjected. The output signal can be electronically processed and read on a meter or some other suitable indicating device. The main accelerometers used in testing for NVH are of piezoelectric material, that can be single crystal, as quartz, and ceramic.

They can measure the acceleration on a single direction, monoaxial, or three directions, three-axial. The kind of accelerometers leveraged in NVH testing are the PCB accelerometers that have the benefit of being miniaturized so they can be inserted in narrow spaces (figure 1.4) [8].

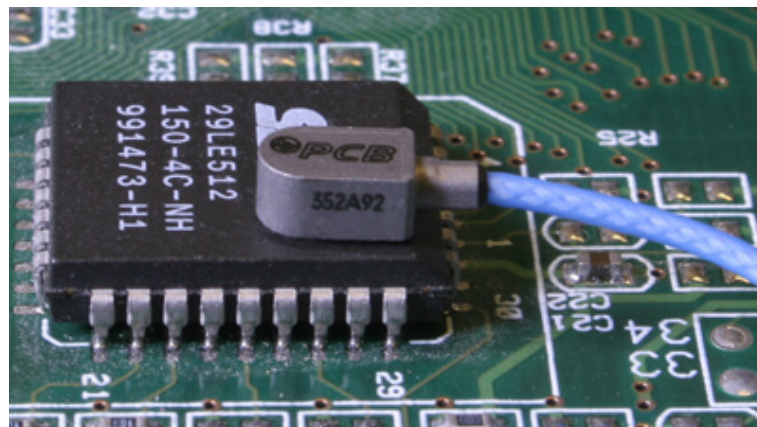


Figure 1.4: Teardrop accelerometer. [8]

- Microphone:

The microphone is the main transducer for acoustic measurements, that convert the pressure fluctuation in an electric signal. There are different kinds of microphones, among them we can find piezoelectric, electret and capacitive ones. The capacitive microphones are widely used for their superior metrologic characteristics [9]. A sample of a microphone is showed in figure 1.5 [10].



Figure 1.5: Capacitive microphone [10].

- Miniature shaker:

A set of different shakers is provided from Siemens PLM (figure 1.6) [11], the miniature shaker is a vibration exciter that can be leveraged to perform accurate structural excitation in a minimum amount of space, providing an ideal exciter for FRF testing from engine components up to full vehicle. Its compact size allows the user to excite systems bearing locations inside power-train components.



Figure 1.6: Miniature shaker for automotive NVH testing [11].

The miniature shaker enables dynamic excitation when conventional shakers have no access and impact hammers are unpractical. The miniature shaker is

especially suitable for those who plan to perform experimental modal analysis (EMA), transfer path analysis (TPA) and frequency-based substructuring (FBS). Among the benefits there are: frequency range covered from 50 Hz to 5000Hz, and that it can enable internal excitation of assemblies and in hard-to-reach locations.

The NVH test is managed also in Computer Aided Engineering (CAE) with the help of simulation tools such as Simcenter 3D or Simcenter Nastran. As a matter of fact the cost arising from the prototypes required for testing and for the modifications of them can be avoided leveraging simulation prototyping and testing of the component to be analyzed.

1.2 Why do we study Dynamic Substructuring

The structural dynamics is a branch of Engineering concerning structural analysis of a physical structure on which dynamic loads are applied. This area is born with the aim to apply dynamic analysis to structures, indeed executing dynamic analysis mean apply modal analysis for frequency domain, find time history or dynamic displacements ensuing from time varying loads [12]. In the field of structural dynamics, Dynamic Substructuring is a tool that has lead great advantages to manage problems arising on it. Dynamic Substructuring has gained popularity as a technique for numerically constructing subcomponents created by several design teams and predicting the dynamic behavior of the finished item. As a matter of fact this kind of tool is ideally suited to the simulation of mechanical vibrations, which has consequences for a variety of product characteristics, including noise/acoustics, fatigue/durability, comfort, and safety. Additionally, Dynamic Substructuring is applicable to any size and frequency scale. Industrial applications ranging from automotive and aeronautical engineering to the construction of wind turbines and high-tech precision machines make extensive use of this paradigm. The heart of substructuring concepts can be found in the field of domain decomposition. It stem from the need of analyze complex problems and reduce them to smaller and more managable problems to its component and to the problem of finding the interface solution. The domains in which it can be leveraged include the physical, modal, state-space domain as well as in time and frequency [13], as it shown in figure 1.7.

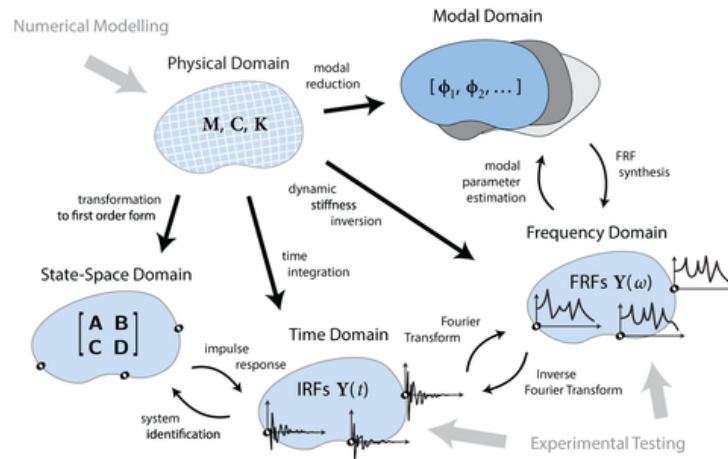


Figure 1.7: Domains of Dynamic Substructuring [13].

The major benefits led from this method are [14]:

1. It allows to assess the dynamic behavior of complex or either too huge structures to be analyzed considering them entirely. When the number of degrees of freedom with which the structure is analyzed is such that the computation time is too large, this method represents a way to reduce it.
2. Local dynamic behavior can be identified more simply by evaluating the subsystems as opposed to the complete system. Consequently, Dynamic Substructuring permits both the identification of local issues and a successful local optimization. Dynamic Substructuring additionally enables the removal of local subsystem behavior that has little bearing on the overall system. As a result, the dynamics of the component are represented simply, which further cuts down on analysis time.
3. The ability to combine modeled parts, analytical or discretized, and experimentally identify components is provided by Dynamic Substructuring.
4. It permits integrating and sharing substructures from several project groups.

Platform techniques are implemented throughout sectors, reusing complex components across all product versions, and the availability of product prototypes for testing and NVH performance evaluation is substantially decreased. In addition, there is a shift toward electric propulsion in the automotive sector, which requires engineers to research novel powertrain concepts with complex load situations and to account for the rising significance of road noise and secondary noise sources. As we discussed Frequency based Dynamic Substructuring, also known as "component transfer path analysis" (C-TPA), is a technological solution to these problems. It

permits modeling a noise source component independent of the structure of the receiver and predicting its behavior when connected to various receivers. This expedites development and significantly enhances design flexibility. The method enables component suppliers to independently characterize their product and forecast the interface interaction with the receiving structure and noise comfort of the finished product. As a result, late troubleshooting, costly troubleshooting activities, and costly design modifications are avoided. Because key expert knowledge is embedded in a model-based development process, it also aids in knowledge retention [15].

1.3 Current industrial problems

NVH and Dynamic Substructuring are actually gaining more importance in different new challenges on the actual industrial developments. The overall transition of the vehicles toward New Energy Vehicles (NEV), so leveraging new and more clean energy sources, require a redesign of the propulsion system and the entire structure. Changing the core components of the systems, as from combustion engine to electric motor in automotive vehicles or hydrogen engine in the aerospace field, require to take in account different sources of vibrations from which also arise a change of the transmission between the components. The electric motor for instance generate loads at different frequencies and amplitudes with respect to the old engines, furthermore the components implemented on an electric motor are different and the amount of them is less, this mean to change perspective during the dynamic analysis.

Nowadays the automotive companies prefer to buy components from suppliers. One of the possible causes of this trend is that the volume of demand is reaching higher level with respect to the last few decades; another cause could be addressed to the cheaper choice of relying on companies that are solely specialized in developing specific components. Furthermore automotive manufacturers of bigger entity are distributed widely on different locations, namely components of a car can be produced and designed on distant area, this require a technical compliance between various locations of the same company. In conjunction with these needs and trends Dynamic Substructuring it is becoming increasingly useful. When integrating dynamic systems, Dynamic Substructuring, in particular Frequency Based Substructuring, is utilized to predict potential noise and vibration difficulties. An overview of FRF Based Substructuring (FBS) is depicted on a web article from Siemens [16]. This technique involve simulation and Computer Aided Engineering, these comes in help also to reduce the cost of testing and the production of prototypes, for instance:

- Components in different physical locations can be assembled virtually.

- Components measured by testing can be assembled using component simulation models.

Considering an electric car, the Frequency Based Substructuring can be useful in order to predict the dynamic behavior of a structure composed by the transmission and the electric motor in a new vehicle body (Figure 1.8) [17].

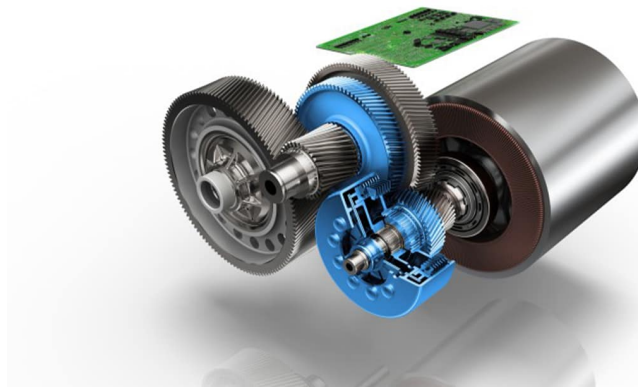


Figure 1.8: Electric motor & transmission [17].

Eventually could exist the need to install the electric motor on a vehicle that has not yet been constructed. In this situation, it may be necessary to comprehend the interaction between the electric motor and a computer simulation model of the new vehicle transmission. Instead of measuring the FRFs in this instance, they might be generated through simulation. To perform FBS, the FRFs obtained from the subsystems should be acquired or simulated under free-free boundary conditions. The advent of the electric propulsion system in the automotive vehicle has led to new challenges to be handled in the NVH area. Different problems arose with the new generation of vehicles such as:

- No masking effect of engine noise: Without the impact of engine noise masking, which is sometimes even desirable in supercars, road/tire/wind/transmission noise are more apparent in NEVs compared to the noise generated from the propulsion system as showed in figure 1.9 from a literature of the Internoise Congress in Innsbruck (2013, Austria)[18].

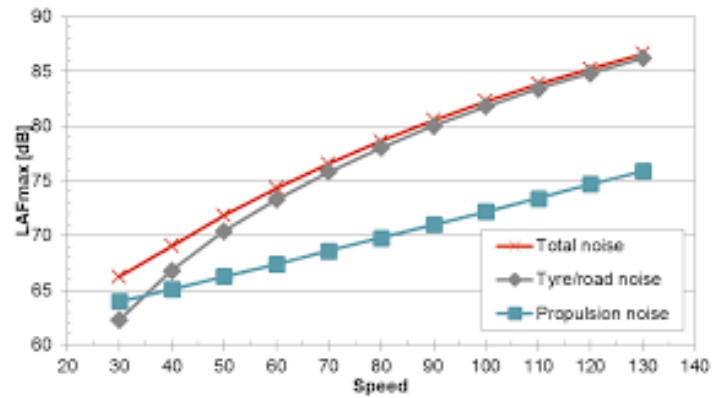


Figure 1.9: The propulsion noise, the tyre/road noise and the total noise from a passenger car calculated with the Nord2000 noise prediction model [18].

For example, transmission noise can no longer "hide" beneath engine noise, therefore buyers will hear the gear noise more easily. Consequently, all vehicle ratings, including subjective driver evaluation and permissible subsystem noise level, must be modified.

- High frequency tonal E-machine noise:

Electric cars can provide a whole new driving experience. In a paper from I.Salleh, M.Z.Md zain & Raja Ishak [19] is compared in the frequency range the noise behaviour of an electric vehicle with respect to ICE vehicles: the high frequency noise is predominant with respect to the low frequency noise, common on cars with internal combustion engine. There is no longer any low-frequency engine noise, but the electric motors produce more high-frequency tone noise, as shown in figure 1.10, furthermore the noise from a ICE vehicle and an Electric vehicle are still comparable at high frequencies.

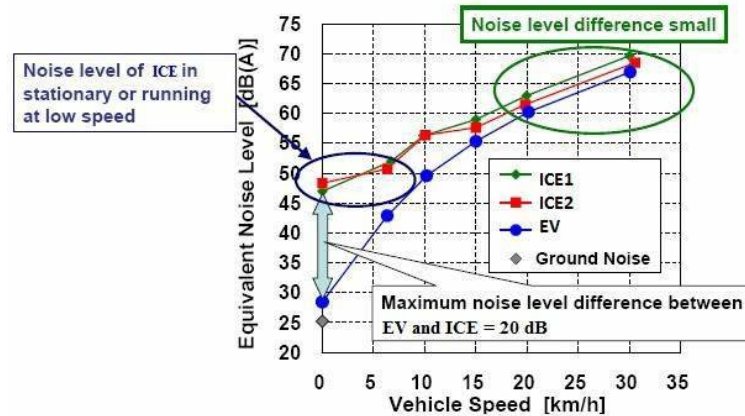


Figure 1.10: Noise level comparison between EV and ICE vehicles at various speeds [19].

Customers can be irritated by the motor howling, which occurs at a low sound pressure level (SPL) yet is plainly audible. Commercially, this issue is the responsibility of the automobile manufacturers, yet there is currently no viable remedy.

- Overall change in the design process require new product knowledge: From the perspective of global dynamics, the entire design is altered: for instance, for a BEV (battery electric vehicle), the global stiffness increases and the damping must be adjusted accordingly. On the other hand, BEVs typically employ a lightweight design for a longer battery life, however the reduced material weight is not advantageous for sound transmission loss. The primary problem at the subsystem level is the noise generated by the e-machine/inverter/transmission. Torque ripple, for instance, is the primary concern in powertrain torsional vibration, and numerous businesses are trying and searching for effective remedies. In addition, the other new electrical components installed to the car will become new noise sources, including start/stop shock, electromagnetic noise, air compressor noise, and so on.

A solution to reduce noise cancellation can be Design Optimization, with CAE design & Bench testing, as well as Active noise cancellation and Passive noise cancellation such as antivibration mounts and acoustic package.

Chapter 2

Theoretical Background

The aim of this chapter is to express the theory and formulation behind the Finite Element Analysis (FEA), as well as to discuss the method of Virtual Point Transformation (VPT), namely these concepts will be the roots of the development for the next sections. The VPT is explained in two types of formulation: the classical one that includes only the translations on the geometry matrices, and the last one that includes a formulation with the geometry matrices extended including the rotational components to improve the prediction of the FRFs along the rotational Degrees of Freedom. Here it is also explained the Modal analysis including theory and formulations of the solvers *SOL103/SOL108/SOL111* implemented on the software Simcenter Nastran.

2.1 Finite Element Analysis

The Finite Element Analysis (FEA) or Finite Element Method (FEM) is a numerical method for solving problems of engineering and mathematical physics. Calculations, models and simulations are used in FEA to predict and comprehend how an object might behave under various physical conditions. Engineers utilize FEA to identify flaws in their design prototypes.

It is useful for problems with complicated geometries, loads and material properties where analytical solutions cannot be obtained. FEA employs the finite element method (FEM), a numerical technique that divides the structure of an object into multiple elements and then reconnects them at nodes. Engineers, developers and other designers can conduct finite element analysis using the algebraic equations generated by the finite element method (FEM).

The Finite Element Analysis is implemented in a wide range of Engineering Fields, as shown in figure 2.1.

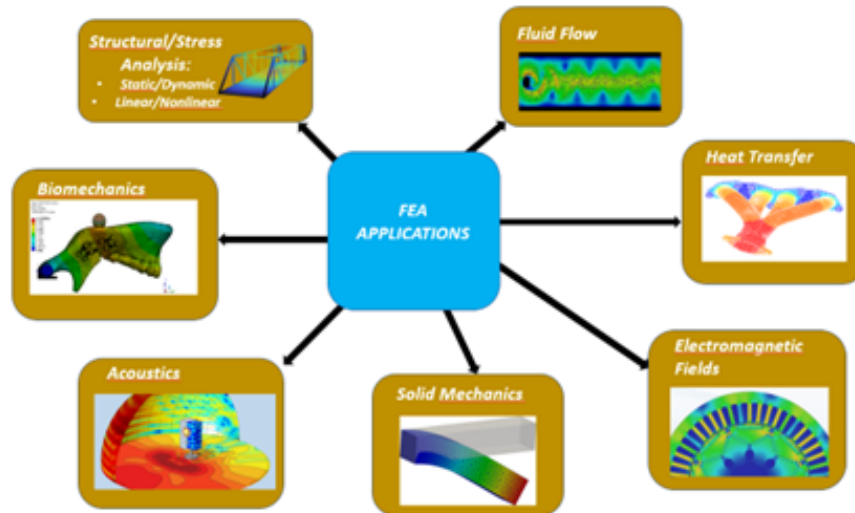


Figure 2.1: Finite Element Analysis applications.

This kind of method paved the way to a more efficient design process. As part of the design process, strength analysis is typically required in mechanical design. Historically, this was accomplished through simple engineering calculations; however, as product performance has become more crucial and designs have become more intricate, these simple methods have become inadequate. With the increase in computational capacity and availability of software that can predict loading for complex geometries and material behavior, the use of the finite element method in both academia and industry has exploded.

There are examples of artifacts designed with their mechanical properties in mind all around us. For instance, the design of a synthetic backbone necessitates knowledge of how the load is distributed between the nearby components of the skeleton, as well as the total load applied to it.

In the process of evaluating the design, all designs must be evaluated for conformity with the specification. Obviously, the specification must be sufficiently detailed to enable the evaluation process to determine which designs comply with the specification and which do not.

The list of areas covered by a typical specification suggests that a variety of evaluation methods may be required. Specifically, the function category may contain:

- Thermal behaviour.
- Strength under load.

- Fluid flow properties.
- Displacement of the structure under load.
- Electrical/Electronic behaviour.

All of these are characteristics of the physical behavior of the design. Regarding the use of the Finite Element Method in mechanical design, the emphasis is on the physical structure design with the intention of supporting an applied load or loads. Furthermore the properties on which the FEM is concerned in the mechanical design are:

- The displacement of parts of the structure when loaded.
- The effect of heat on internal stresses and displacement.
- The optimal thicknesses of material for a given displacement.
- The strength of a structure.
- Crash worthiness.
- The fatigue life of structure.
- The dynamic response of a structure.

2.1.1 Formulation

The formulation of the Finite Element Method is deeply explained from P. Seshu, which is a professor at the Indian Institute of Technology Bombay, in the book "Textbook of Finite Element Analysis" [20]. The Finite Element Method arises from the need of solving the **Boundary value problem**. The Boundary Value Problem is an engineering problem composed from constraints called the **Boundary Conditions (BC)** and a set of differential equations that exploit gradients. Namely in the physical world most of the systems are represented via the gradients, spacing from solid mechanics, fluid mechanics and electromagnetics.

In order to solve the boundary value problem it can be applied an analytical method such as "Direct Integration" and "Laplace transforms" in the case of a simple geometry. In the case of complex geometries it needs to be used a numerical method.

The Finite Element Method (FEM) is a numerical method used to obtain an approximate solution for a given boundary value problem. The outcome of the method is a linear system of equations that are solved using a computer (Gauss elimination algorithm, for example).

The purpose is to find the approximate solution to the boundary value problem, in

this case $\hat{u}(x, y)$ (considering u as the displacement and (x, y) the coordinates of the node along the x -axis and y -axis on which the 2D body is laying), following a "divide and conquer" approach.

The steps followed are showed in figure 2.2:

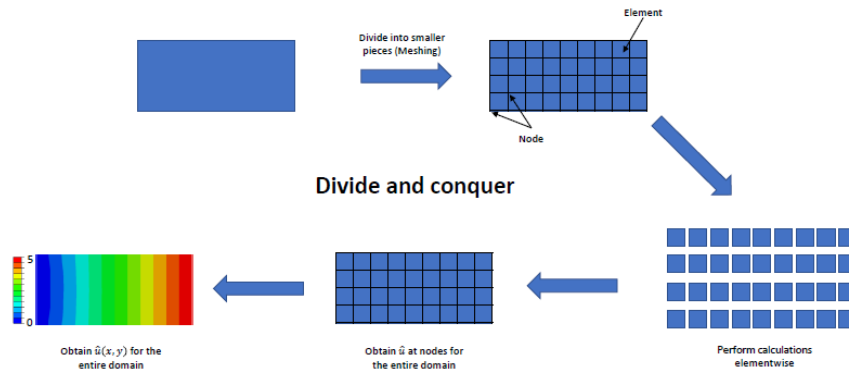


Figure 2.2: Process of FEM.

1. Divide into smaller pieces the geometry, this step is called "meshing".
2. Perform calculations elementwise.
3. Obtain \hat{u} at nodes for the entire domain.
4. Obtain $\hat{u}(x, y)$ for the whole domain.

Mathematical treatment :

In this case it is analyzed a 2D geometry. It is defined Γ as the boundary region, and Ω as the internal region (Figure 2.3).

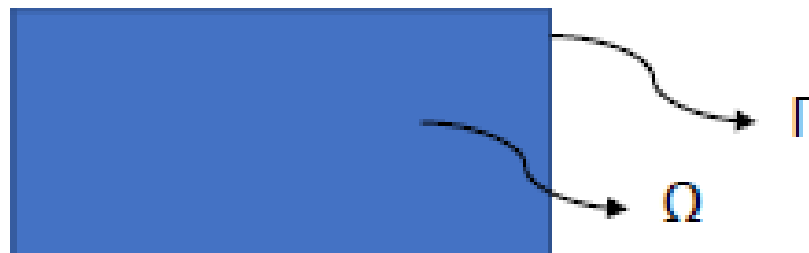


Figure 2.3: Definition of the regions in the geometry.

- We start implementing the Poisson's equation, considering also the boundary conditions:

$$\frac{\partial^2 \mathbf{u}}{\partial^2 \mathbf{x}} + \frac{\partial^2 \mathbf{u}}{\partial^2 \mathbf{y}} = \phi + B.C. \quad (2.1)$$

- We consider $u^e(x, y)$ as the exact solution (Eq. 2.2):

$$\frac{\partial^2 \mathbf{u}^e}{\partial^2 \mathbf{x}} + \frac{\partial^2 \mathbf{u}^e}{\partial^2 \mathbf{y}} - \phi = 0 \quad (2.2)$$

- Obtaining the exact solution is not feasible, so we consider an approximate solution \hat{u} as well as a residual R (Eq. 2.3 & 2.4):

$$\frac{\partial^2 \hat{\mathbf{u}}}{\partial^2 \mathbf{x}} + \frac{\partial^2 \hat{\mathbf{u}}}{\partial^2 \mathbf{y}} - \phi \neq 0 \quad (2.3)$$

$$\mathbf{R} = \frac{\partial^2 \hat{\mathbf{u}}}{\partial^2 \mathbf{x}} + \frac{\partial^2 \hat{\mathbf{u}}}{\partial^2 \mathbf{y}} - \phi \quad (2.4)$$

- In order to find an approximate solution \hat{u} such that the R is close to zero at each point within our domain Ω we apply the **Weighted-Residual method**, that can be expressed in two forms (Eq. 2.5 & 2.6):

$$\int \mathbf{W}(\mathbf{x}, \mathbf{y}) \left(\frac{\partial^2 \hat{\mathbf{u}}}{\partial^2 \mathbf{x}} + \frac{\partial^2 \hat{\mathbf{u}}}{\partial^2 \mathbf{y}} - \phi \right) d\Omega = 0 \quad (2.5)$$

$$\int \mathbf{W}(\mathbf{x}, \mathbf{y}) (\nabla^2 \hat{\mathbf{u}} - \phi) d\Omega = 0 \quad (2.6)$$

Where $W(x, y)$ is a known weight function [20].

- Integrating by parts we obtain the weak form (Eq. 2.7):

$$\int \mathbf{W} \nabla \hat{\mathbf{u}} \cdot \hat{\mathbf{n}} d\Gamma - \int \nabla \mathbf{W} \cdot \nabla \hat{\mathbf{u}} d\Omega - \int \mathbf{W} \phi d\Omega = 0 \quad (2.7)$$

Where $\int \mathbf{W} \nabla \hat{\mathbf{u}} \cdot \hat{\mathbf{n}} d\Gamma$ is the boundary term related to the boundary conditions.

In the end to find the approximate solution we find the equation 2.7, that is defined for the entire domain; whereas for the discretized geometry can be rewritten as in equation 2.8:

$$\int \mathbf{W} \nabla \hat{\mathbf{u}} \cdot \hat{\mathbf{n}} d\Gamma_i - \int \nabla \mathbf{W} \cdot \nabla \hat{\mathbf{u}} d\Omega_i - \int \mathbf{W} \phi d\Omega_i = 0 \quad (2.8)$$

Since each square element is in the continuous domain with the approximated solution $\hat{u}_i(x, y)$, we can reduce the calculation load seeking the solution only in the points that are located in the edges, namely we do a piecewise-interpolation finding a set of solutions \hat{u}_i , as showed in figure 2.4:

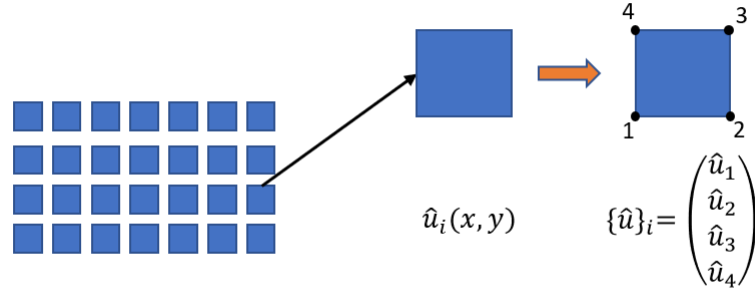


Figure 2.4: FEM from continuous to set of unknowns.

The approximated solution for one element can be expressed as in equation 2.9:

$$\hat{\mathbf{u}}(\mathbf{x}, \mathbf{y}) = \mathbf{N}_1(\mathbf{x}, \mathbf{y})\hat{u}_1 + \mathbf{N}_2(\mathbf{x}, \mathbf{y})\hat{u}_2 + \mathbf{N}_3(\mathbf{x}, \mathbf{y})\hat{u}_3 + \mathbf{N}_4(\mathbf{x}, \mathbf{y})\hat{u}_4 \quad (2.9)$$

Or with the compressed form in equation 2.10:

$$\hat{\mathbf{u}}(\mathbf{x}, \mathbf{y}) = \Sigma \mathbf{N}_k \mathbf{u}_k \text{ or } [\mathbf{N}]\{\mathbf{u}\} \quad (2.10)$$

Where N_k are shape functions: known functions that depends on the shape of the element.

Substituting in the approximated solutions in the equation 2.7 we obtain a linear system of equations for one element (equation 2.11):

$$[\mathbf{k}_i]\{\mathbf{u}\}_i = \{\mathbf{f}\}_i \quad (2.11)$$

Where $[k]_i$ is the linear stiffness matrix and $\{f\}_i$ is the element load vector. The global equation is represented in 2.12, with $[K]$ as the global stiffness matrix and $\{F\}$ as the global force vector.

$$[\mathbf{K}]\{\mathbf{U}\} = \{\mathbf{F}\} \quad (2.12)$$

In the end the number of equations that has to be solved is the same as the number of nodes that we choose to describe our geometry.

2.2 Modal analysis

The study of the dynamic properties of linear structures in the frequency domain is known as Modal analysis. An overview of Modal analysis is depicted on a Siemens-DISW web article [21]. Modal analysis can be based on structural testing or on simulations that use finite element analysis. These dynamic features include resonance frequencies (sometimes termed "natural frequencies" or "eigenfrequencies") and structural modes (or "eigenmodes"). When a structure is subjected to operational loads, the vibration behavior of the structure is determined by its dynamic properties, which in turn are reliant on the mass, stiffness, and damping distribution of the structure. Each and every one of a linear structural system deformations can be described as a linear combination of the system structural modes, which together make up an orthonormal vector basis.

Data capture and additional analysis are both part of the modal testing process. The entire procedure is frequently referred to as modal testing and analysis or experimental modal analysis when it is used in an industrial setting (EMA).

The outcomes of modal testing and analysis are utilized in a variety of simulation and testing applications, such as vibration response calculations, root cause analysis of vibration problem, and damage detection, as well as for adding flexibility to multibody analysis and accelerating durability and vibro-acoustic simulations. Modal-based calculations are highly effective and permit rapid evaluation of structural changes in response to any stimulus.

Modal analysis implemented with structural testing or finite element analysis simulations in CAE lead to various benefits:

- Understand the behaviour of a structure under vibrations.
- Boost the speed of vibro-acoustic, structural and durability calculations.
- Correlate and update simulation models
- Include flexibility in multibody simulation models.

2.2.1 Formulation

One of the purposes for which we analyze the dynamic behavior of a structure is the need to solve noise and vibration problems ensuing from the resonance phenomena, in which the forces acting on the body can excite one or more modes of vibration. Indeed the modes of vibration lying in the frequency range of the loads applied on the structure are possible sources of problems. The formulation of Modal analysis take citations from the article by "Structural Testing" from Brüel Kjaer [22].

The free or forced dynamic response of a structure can be reduced to a discrete set of modes. The modes of a structure can be described from three specific parameters:

- Modal frequency
- Modal damping
- Mode shape

With these three parameters we can depict exhaustively the dynamic behavior of a structure in the frequency range in which we are interested, describing each mode leveraging them. Furthermore the modes of vibration represent the inherent dynamic properties of a free structure, that is a structure on which there are no forces acting. For each mode the body will have a different mode shape describing the deformation of it, combining the mode shapes in the frequency range of interest we have the complete dynamic behavior in the physical domain as showed in figure 2.5.

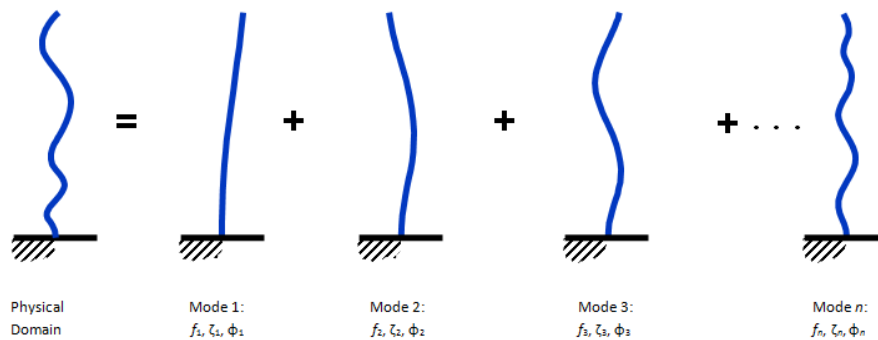


Figure 2.5: Decomposition in modes of the structure of the dynamic behavior.

Modal analysis can be executed either through analytical or experimental techniques, it is the process of determining all the modal parameters in order to formulate a mathematical dynamic model.

Mathematical models can bring some advantages:

- To gain a better comprehension of how structures behave under dynamic loads.
- To be leveraged in data reduction and smoothing techniques as curve fitting.
- To simulate changing dynamic characteristics ensuing from possible physical modifications.

The main feature is that they model and represent the structure dynamic behaviour, constrained by a set of assumptions and boundary conditions. The **analytical mathematical models** are founded on the mass and stiffness distributions of a particular set of boundary conditions. Typically, these calculations are performed

using the Finite Element Method (FEM), and the model generates a massive set of coupled differential equations that can only be solved by utilizing powerful computers. Whereas from measured modal data, which represent the system under the measured conditions, **experimental mathematical models** can be developed. Typically, the model consists of a set of independent differential equations, one for each measurement mode. This model is commonly known as the "Modal Model".

The Frequency Response Function:

One really efficient model of a linear system is a frequency domain model, in which the output spectrum is expressed as the input spectrum weighted by a system descriptor, as showed in equation 2.13.

$$\mathbf{X}(\omega) = \mathbf{H}(\omega) \cdot \mathbf{F}(\omega) \tag{2.13}$$

Where $\mathbf{H}(\omega)$ is called the **Frequency response function** (FRF), and it is defined in equation 2.14.

$$\mathbf{H}(\omega) = \frac{\mathbf{X}(\omega)}{\mathbf{F}(\omega)} \tag{2.14}$$

The equation 2.14 depict a complex ratio between output and input, as a function of the frequency expressed by ω . Namely the descriptor considered as a complex entity has a magnitude $|\mathbf{H}(\omega)|$ and a phase $\angle \mathbf{H}(\omega) = \phi(\omega)$.

The FRF represent a sinusoidal input force with a frequency ω that produce a sinusoidal output motion at the same frequency. The output amplitude ensue from a gain of $|\mathbf{H}(\omega)|$, whereas the phase between the output and the input is shifted of $\angle \mathbf{H}(\omega)$.

2.2.2 Modal frequency response

In order to compute the Dynamic response of a structure in the frequency domain, a "frequency response analysis" is needed [23]. The frequency response analysis is leveraged to calculate the structural response to steady state oscillatory excitation. The excitation is defined explicitly in the frequency domain, in addition it can be in the form of applied forces and enforced motions, such as displacements, velocities or accelerations. There are two types of frequency response analysis, in the software Simcenter Nastran they are exploited with two kind of solvers respectively:

- **SOL 108** for the "Direct frequency response analysis [24].
- **SOL 111** for the "Modal frequency response analysis [25].

These two kind of frequency response analysis have different approach and formulations depicted deeply in the Siemens NX User Guide[24,25]:

1. **Direct Frequency Response analysis:** In this analysis the structural response is computed at discrete excitation frequencies by solving a set of coupled matrix equations using complex algebra. The equation of motion for a damped system subjected to a harmonic excitation is showed in equation 2.15.

$$[\mathbf{M}]\{\ddot{\mathbf{x}}(\mathbf{t})\} + [\mathbf{B}]\{\dot{\mathbf{x}}(\mathbf{t})\} + [\mathbf{K}]\{\mathbf{x}(\mathbf{t})\} = \{\mathbf{P}(\omega)\}e^{i\omega t} \quad (2.15)$$

In the equation $[M]$, $[B]$ and $[K]$ are respectively the mass-matrix, viscous damping matrix and stiffness matrix. $\{\ddot{x}(t)\}$, $\{\dot{x}(t)\}$ and $\{x(t)\}$ represents the acceleration, velocity and displacement vectors. Furthermore the load $\mathbf{P}(\omega)$ is a complex vector, that is convenient for the mathematical solution of the problem, even if from a physical point of view the load can be both real or imaginary. The same interpretation is used for response quantities. For harmonic motion, that is the basis of a frequency response analysis, it is assumed a harmonic solution depicted in equation 2.16.

$$\{\mathbf{x}\} = \{\mathbf{u}(\omega)\}e^{i\omega t} \quad (2.16)$$

In equation 2.16 $\{\mathbf{u}(\omega)\}$ is a complex displacement vector. Taking the first and the second derivative of the equation 2.16 we can retrieve the complex velocity vector and the complex acceleration vector respectively in equation 2.17 and 2.18.

$$\{\dot{\mathbf{x}}\} = i\omega\{\mathbf{u}(\omega)\}e^{i\omega t} \quad (2.17)$$

$$\{\ddot{\mathbf{x}}\} = -\omega^2\{\mathbf{u}(\omega)\}e^{i\omega t} \quad (2.18)$$

Substituting equation 2.16, 2.17, 2.18 in equation 2.15 we can find equation 2.19.

$$-\omega^2[\mathbf{M}]\{\mathbf{u}(\omega)\}e^{i\omega t} + i\omega[\mathbf{B}]\{\mathbf{u}(\omega)\}e^{i\omega t} + [\mathbf{K}]\{\mathbf{u}(\omega)\}e^{i\omega t} = \{\mathbf{P}(\omega)\}e^{i\omega t} \quad (2.19)$$

After dividing by $e^{i\omega t}$, the equation 2.19 become simplified in the form of the equation 2.20.

$$[-\omega^2\mathbf{M} + i\omega\mathbf{B} + \mathbf{K}]\{\mathbf{u}(\omega)\} = \{\mathbf{P}(\omega)\} \quad (2.20)$$

The frequency response is obtained by solving equation 2.20 for $\{\mathbf{u}(\omega)\}$ at various forcing frequencies ω .

2. Modal Frequency Response Analysis: This is an alternate method to compute the frequency response. This method is based on uncoupling the equations of motion when no damping or only modal damping is used, exploiting the mode shapes of the structure. Furthermore depending on the number of modes computed and retained, it reduces the problem size. Both of these features allow the modal frequency response analysis more efficient on the computational side with respect to the direct way. One advantage is that this method replaces the physical DoFs with a reduced number or modal DoFs. Indeed if we have less DoFs we have a more fast solution, specifically the *SOL108* solve the equations for each discrete frequency, whereas the *SOL111* solve the analysis from a subset of modes so reducing the computational effort. Since modal frequency response analysis uses the mode shapes of a structure, modal frequency response analysis is a natural extension of normal modal analysis. For the modal frequency response analysis we have to neglect the viscous and structural damping in equation 2.15, so it simplifies to equation 2.21.

$$[\mathbf{M}]\{\ddot{\mathbf{x}}(\mathbf{t})\} + [\mathbf{K}]\{\mathbf{x}(\mathbf{t})\} = \{\mathbf{P}(\omega)\}e^{i\omega t} \quad (2.21)$$

It is assumed also a harmonic solution as represented on equation 2.19. Thereafter in equation 2.21 it is neglected the forcing term and substituted the equation 2.16 plus the equation 2.19. Then solving the resulting equation yields the natural frequencies and mode shapes for the system. After this step there are implemented the mode shapes $[\phi]$ to transform the response from physical coordinates, $\{\mathbf{u}(\omega)\}$, to modal coordinates $\{\boldsymbol{\xi}(\omega)\}$, as showed in equation 2.22.

$$\{\mathbf{x}\} = [\phi]\{\boldsymbol{\xi}(\omega)\}e^{i\omega t} \quad (2.22)$$

Equation 2.22 represents an equality if all modes are calculated and used. Instead when a subset of all modes are calculated or used, equation 2.22 represent an approximation. Substituting equation 2.22 and the second derivative time of it into equation 2.21 and simplifying yields the equation of motion 2.23 in terms of the modal coordinates.

$$-\omega^2[\mathbf{M}][\phi]\{\boldsymbol{\xi}(\omega)\} + [\mathbf{K}][\phi]\{\boldsymbol{\xi}(\omega)\} = \{\mathbf{P}(\omega)\} \quad (2.23)$$

The equations forming 2.23 are coupled. The equation 2.23 has to be premultiplied by the transpose of the eigenvector matrix $[\phi]^T$ in order to uncouple the equations, as showed in equation 2.24.

$$-\omega^2[\phi]^T[\mathbf{M}][\phi]\{\boldsymbol{\xi}(\omega)\} + [\phi]^T[\mathbf{K}][\phi]\{\boldsymbol{\xi}(\omega)\} = [\phi]^T\{\mathbf{P}(\omega)\} \quad (2.24)$$

We have diagonalized with this step the mass and stiffness matrices. The transformed mass and stiffness matrices and forcing vector are referred to as:

$$[\phi]^T[\mathbf{M}][\phi] = \text{Modal (generalized) mass matrix.} \quad (2.25)$$

$$[\phi]^T[\mathbf{K}][\phi] = \text{Modal (generalized) stiffness matrix.} \quad (2.26)$$

$$[\phi]^T\{\mathbf{P}\} = \text{Modal force vector.} \quad (2.27)$$

In the uncoupled form, the equation of motion can be written as a set of single degree of freedom systems as showed in equation 2.28.

$$-\omega^2 m_i \xi_i(\omega) + k_i \xi_i(\omega) = p_i(\omega) \quad (2.28)$$

Where m_i is the modal mass for the i^{th} mode, k_i is the modal stiffness for the i^{th} mode and p_i is the modal force for the i^{th} mode. From equation 2.28 the individual modal responses represented from $\xi_i(\omega)$ are calculated for a specific forcing frequency ω . The physical response at the specified forcing frequency is then recovered from equation 2.22.

2.3 Virtual Point Transformation

The Dynamic Substructuring is among the approaches in Engineering that fulfills the need to analyze a complex system, with the procedure of reducing it to small systems that have to be analyzed singularly. Its main features are exploited in the mechanical engineering area, specifically to study the dynamic response of a complete system composed by subsystems or to study a single component. Analyzing the dynamic of a subsystem can be exploited in cases which starting from the split of the complex system the isolated subsystems have to be designed from different teams; furthermore evaluating the design separately can lead to a boost in the optimization of the design, wherever the geometrical complexity is too high.

The results ensuing from the utilization of Dynamic Substructuring are proven to be effective with analytical or numerical data, on the contrary there are still problems with experimental data as showed by D. de Klerk in various papers [26], [27], [28]. Considering the Dynamic Substructuring in the frequency domain there are ongoing methods that are trying to improve the implementation with experimental data. Firstly the Frequency Based Substructuring (FBS) knowed also as "Impedance coupling" or "Admittance modeling" was developed by Jetmundsen

et al. [29]. Afterward it was improved by de Klerk et al. in 2006 with the Lagrange Multiplier Frequency Based Substructuring method (LM FBS) [30]. Interface modeling and producing a full-DoFs frequency-response-functions (FRFs) matrix including translational and rotational DoFs provide the greatest difficulty in LM FBS coupling. The LM FBS formulation also necessitates that the interface DoFs are collocated on both substructures, which is not always possible in practice. For a discrete interface, the addition of rotational degrees of freedom and the collocation of the interface degrees of freedom can be solved with a technique known as virtual point transformation (VPT)[31]. Many transformation efforts have examined the translational degrees of freedom on so-called interface deformation modes (IDMs), which are thought to characterize the interface dynamic behavior. Furthermore, as shown in [32], the interface can be modeled as rigid or extended with a flexible interface mode. The theoretical description of the formulation reported take concepts from the paper "Including directly measured rotations in the virtual point transformation"[33].

2.3.1 Formulation using translation

In this section it is briefly reported the LM FBS method [34], thereafter the formulation of the virtual point transformation and how it is implemented to fulfill the difficulties that cannot be overtaken by the LM FBS method. The theory that constitute the VPT is cited from the work of M.V. van der Seijs et a.[35]. In frequency-based substructuring (FBS), from the separate admittances of two substructures \mathbf{Y}^A and \mathbf{Y}^B we can retrieve the admittance of the assembled system \mathbf{Y}^{AB} , as showed in figure 2.6.

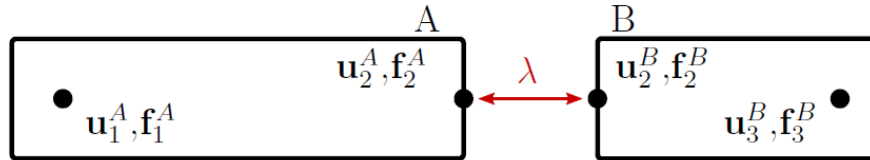


Figure 2.6: Schematic representation of the substructuring problem.

Thus we retrieve the governing equation of motion for two uncoupled substructures in equation 2.29.

$$\mathbf{Y}^{A|B}(\mathbf{f} + \mathbf{g}) = \begin{bmatrix} \mathbf{Y}_{11}^A & \mathbf{Y}_{12}^A & 0 & 0 \\ \mathbf{Y}_{21}^A & \mathbf{Y}_{22}^A & 0 & 0 \\ 0 & 0 & \mathbf{Y}_{22}^B & \mathbf{Y}_{23}^B \\ 0 & 0 & \mathbf{Y}_{32}^B & \mathbf{Y}_{33}^B \end{bmatrix} \left(\begin{bmatrix} \mathbf{f}_1^A \\ \mathbf{f}_2^A \\ \mathbf{f}_2^B \\ \mathbf{f}_3^B \end{bmatrix} + \begin{bmatrix} 0 \\ \mathbf{g}_2^A \\ \mathbf{g}_2^B \\ 0 \end{bmatrix} \right) = \begin{bmatrix} \mathbf{u}_1^A \\ \mathbf{u}_2^A \\ \mathbf{u}_2^B \\ \mathbf{u}_3^B \end{bmatrix} = \mathbf{u} \quad (2.29)$$

Where \mathbf{f} is the vector of external forces, \mathbf{u} denotes the displacements and \mathbf{g} is the vector of interface forces between the two substructures in the coupled state. In order to obtain a coupling between the two substructures we need to define a connection between them and fulfill the conditions of compatibility and equilibrium showed in equation 2.30 and 2.31.

$$\mathbf{B}\mathbf{u} = \mathbf{0} \quad (2.30)$$

$$\mathbf{g} = -\mathbf{B}^T\boldsymbol{\lambda} \quad (2.31)$$

Where \mathbf{B} is a signed Boolean matrix and $\boldsymbol{\lambda}$ are Lagrange multipliers representing the reaction forces. Thereafter inserting equations 2.30 and 2.31 in equation 2.29 and eliminating $\boldsymbol{\lambda}$ yields the admittance matrix of the assembled system in the equation 2.32.

$$\mathbf{Y}^{\mathbf{A}\mathbf{B}}\mathbf{f} = \left(\mathbf{Y}^{A|B} - \mathbf{Y}^{A|B}\mathbf{B}^T(\mathbf{B}\mathbf{Y}^{A|B}\mathbf{B}^T)^{-1}\mathbf{B}\mathbf{Y}^{A|B} \right) \mathbf{f} = \mathbf{u} \quad (2.32)$$

Frequently the two substructures cannot be directly coupled with the LM FBS method in the case where the sensors and the excitation points are not in the same positions considering both of them. Namely the LM FBS method is based on a full-DOF response model, with collocated interface degrees of freedom. The advantageous feature of the virtual point transformation is that it can enable the coupling of two substructures with non-collocated interface DoFs; namely following the method it can be chosen a virtual point, that in this case is located close to the physical interface of the substructures, and can be projected the force inputs and the measured sensor displacements on the IDMs. Assuming only the rigid-body IDMs then we have $m = 6$ DoFs for each virtual point, considering 3 DoFs for translations plus 3 DoFs for rotations. Furthermore, in the case of connections with more complexity, the flexible deformation modes [36] can be also added. The achieved transformation is showed in the equation 2.33.

$$\mathbf{Y}_{qm} = \mathbf{T}_u\mathbf{Y}_{22}\mathbf{T}_f^T \quad (2.33)$$

Where \mathbf{Y}_{qm} is the virtual point FRF matrix with a perfectly collocated force and displacement DoF, that allows to couple the two substructures following the LM FBS method; \mathbf{Y}_{22} it is the admittance FRF of the non-collocated interface DoFs, so \mathbf{u}_2^A and \mathbf{u}_2^B ; \mathbf{T}_u is the displacement transformation matrix and \mathbf{T}_f is the force transformation matrix. Thereafter the **Interface displacement reduction** and the **Interface force reduction** are described.

- **Interface displacement reduction**

With a set of interface displacement modes (IDMs) it can be achieved the interface displacement reduction. The IDMs are contained in the matrix $\mathbf{R}_u \in \mathbb{R}^{n_u \times m}$. The purpose of the reduction is to reduce n_u measured interface displacements with m IDMs. It can be considered as a case study the interface connection showed in figure 2.7.

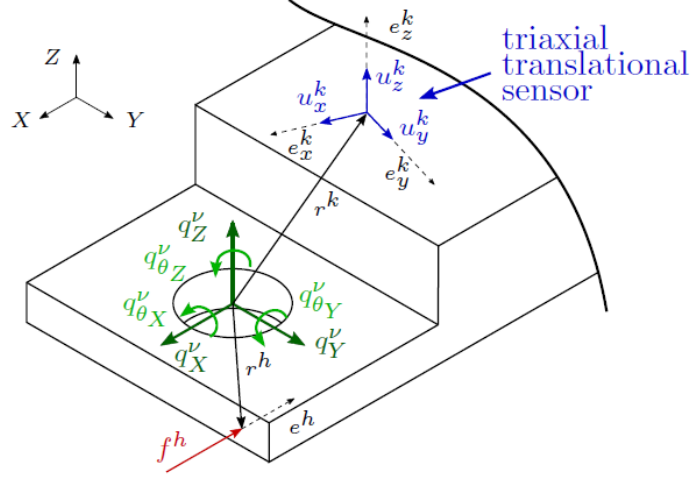


Figure 2.7: Example of interface connection with VP and triaxial translation sensor.

Considering only the rigid IDMs, the VP has 6 DoFs composed by three translations $q_t^\nu = [q_X^\nu, q_Y^\nu, q_Z^\nu]$ and three rotations $q_\theta^\nu = [q_{\theta_X}^\nu, q_{\theta_Y}^\nu, q_{\theta_Z}^\nu]$, where ν represent a specific VP on the substructure. If it is known the sensor orientation as well as the location, it can be retrieved the kinematic relation between the virtual point DoF q^ν and the sensor displacement u^k (equation 2.34).

$$\begin{bmatrix} u_x^k \\ u_y^k \\ u_z^k \end{bmatrix} = \begin{bmatrix} e_{x,X}^k & e_{x,Y}^k & e_{x,Z}^k \\ e_{y,X}^k & e_{y,Y}^k & e_{y,Z}^k \\ e_{z,X}^k & e_{z,Y}^k & e_{z,Z}^k \end{bmatrix} \begin{bmatrix} 1 & 0 & 0 & 0 & r_Z^k & -r_Y^k \\ 0 & 1 & 0 & -r_Z^k & 0 & r_X^k \\ 0 & 0 & 1 & r_Y^k & -r_X^k & 0 \end{bmatrix} \begin{bmatrix} q_X^\nu \\ q_Y^\nu \\ q_Z^\nu \\ q_{\theta_X}^\nu \\ q_{\theta_Y}^\nu \\ q_{\theta_Z}^\nu \end{bmatrix} + \begin{bmatrix} \mu_{u_x}^k \\ \mu_{u_y}^k \\ \mu_{u_z}^k \end{bmatrix} \quad (2.34)$$

In the equation 2.34 the vector $\boldsymbol{\mu}_u^k$ contains any residual motion that is not included in the subspace of IDMs, whereas the vector $[e_{x,X}^k, e_{y,X}^k, e_{z,X}^k]^T$ represents the coordinates of the unit direction X of sensor k represented in the global reference frame of the structure. If in the frequency range considered it can be done the hypothesis of rigidity, then the residual motion represented by $\boldsymbol{\mu}_u^k$ can be neglected. The equation 2.34 can be expanded in order to include all the measured displacement, leading to equation 2.35.

$$\mathbf{u} = \mathbf{R}_u \mathbf{q} + \boldsymbol{\mu}_u \quad (2.35)$$

With the aim to increase the control on the transformation it is implemented the symmetrical weighting matrix \mathbf{W}_u , then the equation is solved in a least-mean-square sense (minimizing the \mathbf{W}_u -norm of the residual) for \mathbf{q} (equation 2.36).

$$\mathbf{q} = (\mathbf{R}_u^T \mathbf{W}_u \mathbf{R}_u)^{-1} \mathbf{R}_u^T \mathbf{W}_u \mathbf{u} \quad (2.36)$$

Thus the residual displacement is retrieved in equation 2.37.

$$\mathbf{R}_u^T \mathbf{W}_u \boldsymbol{\mu}_u = \mathbf{0} \quad (2.37)$$

Furthermore the equation 2.36 can be simplified in equation 2.38, where the transformation matrix \mathbf{T}_u can be expressed as in equation 2.39.

$$\mathbf{q} = \mathbf{T}_u \mathbf{u} \quad (2.38)$$

$$\mathbf{T}_u \triangleq (\mathbf{R}_u^T \mathbf{W}_u \mathbf{R}_u)^{-1} \mathbf{R}_u^T \mathbf{W}_u \quad (2.39)$$

- **Interface force reduction**

Considering figure 2.7, the force f^h will lead to a virtual load \mathbf{m}^ν applied on the virtual point ν . Considering the reduction of the forces at the interface it is derived a similar matrix containing the IDMs, as showed in equation 2.40.

$$\begin{bmatrix} m_X^\nu \\ m_Y^\nu \\ m_Z^\nu \\ m_{\theta_X}^\nu \\ m_{\theta_Y}^\nu \\ m_{\theta_Z}^\nu \end{bmatrix} = \begin{bmatrix} 1 & 0 & 0 \\ 0 & 1 & 0 \\ 0 & 0 & 1 \\ 0 & -r_Z^h & r_Y^h \\ r_Z^h & 0 & -r_X^h \\ -r_Y^h & r_X^h & 0 \end{bmatrix} \begin{bmatrix} e_X^h \\ e_Y^h \\ e_Z^h \end{bmatrix} \mathbf{f}^h. \quad (2.40)$$

Furthermore the equation 2.40 can be rewritten in synthetic form (equation 2.41), combining before the n_f input forces.

$$\mathbf{m} = \mathbf{R}_f^T \mathbf{f} \quad (2.41)$$

In equation 2.41 the matrix that include the IDMs is $\mathbf{R}_f^T \in \mathbb{R}^{m \times n_f}$. In order to proceed with the virtual point transformation, it has to be built the force transformation matrix \mathbf{T}_f^T . The equation 2.41 is often under-determined because of $n_f \geq m$; thus the inversion is obtained with the weighted right inverse of \mathbf{R}_f^T (i.e. finding a solution that has a minimal \mathbf{W}_f -norm) as showed in equation 2.42:

$$\tilde{\mathbf{f}} = \mathbf{W}_f \mathbf{R}_f (\mathbf{R}_f^T \mathbf{W}_f \mathbf{R}_f)^{-1} \mathbf{m} \quad (2.42)$$

Where \mathbf{W}_f is a symmetrical weighting matrix. Equation 2.42 can be further rewritten as the equation 2.43, where we can make the assumption of equation 2.44.

$$\tilde{\mathbf{f}} = \mathbf{T}_f^T \mathbf{m} \quad (2.43)$$

$$\mathbf{T}_f^T \triangleq \mathbf{W}_f \mathbf{R}_f (\mathbf{R}_f^T \mathbf{W}_f \mathbf{R}_f)^{-1} \quad (2.44)$$

2.3.2 Formulation using translation and rotation

One of the challenges of the virtual point transformation is the reconstruction of the rotational response. Since it is an indirect method it can lead to erroneous results. Even though with the virtual point transformation the reconstruction of the translational response is proven to be effective and accurate, the reproduction of the rotational DoFs shows a lower quality [37]. The output signal from the translation movement sometimes masks the signal from the rotating movement, which is one of the reasons [38]. Thereafter it is reported a practical example to demonstrate the errors ensuing from small deviations in the sensor sensitivity. This is a numerical simulation of a cantilever beam (Figure 2.8), with two translation sensors located on the free end of the beam. They measure respectively the translations u_1 and u_2 , furthermore the rotation θ is retrieved with finite differences.

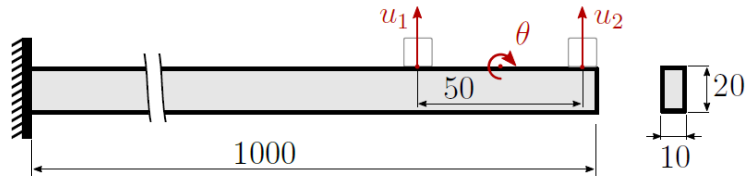


Figure 2.8: Case of a cantilever beam with two translation sensors placed on the free end.

The results are comparing a response with and without a 5% calibration inaccuracy. In figure 2.9a it can be seen that for the translational response there is not inaccuracy, so it is not influenced, whereas for the rotational response in figure 2.9b we can see that it leads to a loss of accuracy.

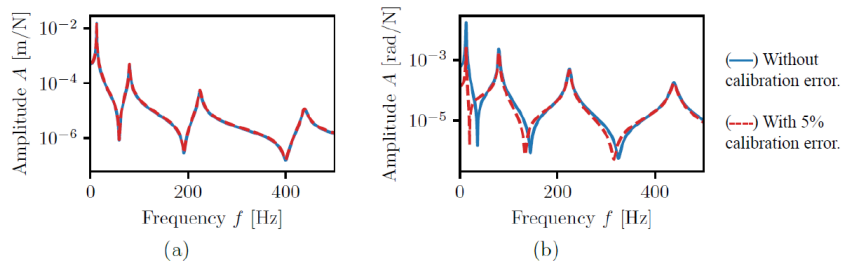


Figure 2.9: Effect of calibration error in the sensor sensitivity: a) translational FRF Y_{u_2} ; b) rotational FRF Y_{θ} [32].

Even though the VPT is an indirect method and the quality in the application can be influenced from this kind of inaccuracies, the errors can still be contained since the number of measured DoFs is often larger than the number of IDMs. As a consequence the transformation is overdetermined, so with the least-squares fit the errors on a single sensor are decreased. However small inaccuracies due to the sensor location and the sensitivity of it can be relevant. A way to increase the accuracy of the VPT on the rotational DoFs in the interface is to expand the formulation from data gathered by a triaxial rotation sensor (as showed in figure 2.10): the measured rotational response is projected onto the interface deformation modes to obtain the collocated VP FRF Matrix.

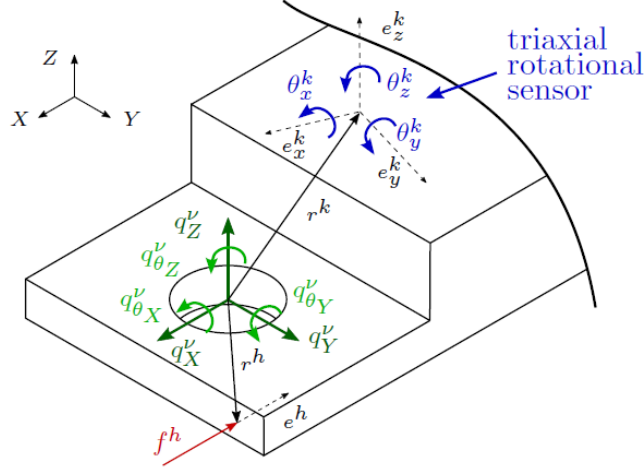


Figure 2.10: Example of the interface with virtual point and a triaxial rotational sensor.

The kinematic equation 2.45 can be formulated considering the virtual point DoF \mathbf{q}^ν and the sensor rotation $\boldsymbol{\theta}^k$. From the formulation ensue that only the rotational DoF of the virtual point are influenced from the measurements of the triaxial rotational sensor.

$$\begin{bmatrix} \theta_x^k \\ \theta_y^k \\ \theta_z^k \end{bmatrix} = \begin{bmatrix} e_{x,X}^k & e_{x,Y}^k & e_{x,Z}^k \\ e_{y,X}^k & e_{y,Y}^k & e_{y,Z}^k \\ e_{z,X}^k & e_{z,Y}^k & e_{z,Z}^k \end{bmatrix} \begin{bmatrix} 0 & 0 & 0 & 1 & 0 & 0 \\ 0 & 0 & 0 & 0 & 1 & 0 \\ 0 & 0 & 0 & 0 & 0 & 1 \end{bmatrix} \begin{bmatrix} q_X^\nu \\ q_Y^\nu \\ q_Z^\nu \\ q_{\theta_X}^\nu \\ q_{\theta_Y}^\nu \\ q_{\theta_Z}^\nu \end{bmatrix} + \begin{bmatrix} \mu_{\theta_x}^k \\ \mu_{\theta_y}^k \\ \mu_{\theta_z}^k \end{bmatrix} \quad (2.45)$$

With $\boldsymbol{\mu}_\theta^k$ as the vector that contains any residual motion, that can be neglected if we can do the assumption of rigidity. Furthermore the equation 2.45 can be expanded in equation 2.46 in order to include the whole set of directly measured rotations.

$$\boldsymbol{\theta} = \mathbf{R}_\theta \mathbf{q} + \boldsymbol{\mu}_\theta. \quad (2.46)$$

As it can be seen the equation 2.45 depends only on the sensor orientation, whereas the kinematic equation for the translation depends also on the sensor location. Equation 2.35 and 2.45 can be reformulated in a combined form for all the measured translational and rotational displacements in the equation 2.47.

$$\begin{bmatrix} \mathbf{u} \\ \boldsymbol{\theta} \end{bmatrix} = \begin{bmatrix} \mathbf{R}_u \\ \mathbf{R}_\theta \end{bmatrix} \mathbf{q} + \begin{bmatrix} \boldsymbol{\mu}_u \\ \boldsymbol{\mu}_\theta \end{bmatrix} = \mathbf{R}_{\mathbf{u},\boldsymbol{\theta}} \mathbf{q} + \boldsymbol{\mu}_{\mathbf{u},\boldsymbol{\theta}}. \quad (2.47)$$

To solve the equation 2.47 for \mathbf{q} in a minimal-quadratic way, it is minimized the norm of the weighted residuals on the displacements and rotations in equation 2.48:

$$\mathbf{q} = \mathbf{argmin} \left(\begin{bmatrix} \boldsymbol{\mu}_u \\ \boldsymbol{\mu}_\theta \end{bmatrix}^T \mathbf{W}_{u,\theta} \begin{bmatrix} \boldsymbol{\mu}_u \\ \boldsymbol{\mu}_\theta \end{bmatrix} \right) \text{ where } \mathbf{W}_{u,\theta} = \mathbf{diag} [\mathbf{W}_u, \mathbf{W}_\theta]. \quad (2.48)$$

The rotations of the VP are not solely determined by the rotational DoFs in this approach. Namely the virtual point rotations have influence on the translation residual (as showed in equation 2.34), also the DoFs computed from equation 2.48 for the virtual point minimize $\boldsymbol{\mu}_u^T \mathbf{W}_u \boldsymbol{\mu}_u + \boldsymbol{\mu}_\theta^T \mathbf{W}_\theta \boldsymbol{\mu}_\theta$. Thus if less than three rotations are directly measured for the virtual point, the rotational DoFs can still be estimated. To evaluate the residuals from the translation and the rotational sensors in a comparable norm, a proper weighting matrix for the rotations should be used, since equation 2.48 minimizes the residual ensuing from both the kind of sensors. Take into account that the rotational measurement around x axis at rotation sensor k has a residual $\mu_{\theta_x}^k$. If the virtual point would be given that residual rotation, the sensor would be exposed to a displacement $\mu_{\theta_x}^k I_x^k$. I_x^k is represented by $\sqrt{r_y^2 + r_z^2}$, that is the distance among the x axis across the virtual point and the sensor location. A similar logic can be applied to the rotational residuals around the other axes, as well as to each additional rotational sensor. If the norm of global displacements caused by rotating residuals at the VP is to be minimized, the following rotational weighting matrix must be applied:

$$\mathbf{W}_\theta = \mathbf{diag} \left[(I_x^k)^2, (I_y^k)^2, (I_z^k)^2, \dots \right] \quad (2.49)$$

Implementing the equation 2.49 we can solve equation 2.47 for \mathbf{q} obtaining also the combined transformation matrix $\mathbf{T}_{u,\theta}$, leading to equation 2.50 and 2.51.

$$\mathbf{q} = \mathbf{T}_{u,\theta} \begin{bmatrix} \mathbf{u} \\ \boldsymbol{\theta} \end{bmatrix} \quad (2.50)$$

$$\mathbf{T}_{u,\theta} \triangleq (\mathbf{R}_{u,\theta}^T \mathbf{W}_{u,\theta} \mathbf{R}_{u,\theta})^{-1} \mathbf{R}_{u,\theta}^T \mathbf{W}_{u,\theta} \quad (2.51)$$

The suggested combined weighting matrix minimizes the norm of the displacement residuals for each translation sensor and the norm of the overall displacement caused by the rotation residual at the virtual point for each rotational sensor. Thus, the residuals from the rotational and translation sensors can be compared and equation 2.48 is consistent (assuming \mathbf{W}_u is taken as identity).

Chapter 3

Applications of Modal analysis and VPT

This chapter has the purpose to show and validate the applications of **modal analysis** as well as the **virtual point transformation**. Firstly the modal analysis is applied to a cantilever beam, using the Real eigenvalue analysis (SOL 103), Direct frequency response analysis (SOL 108) and Modal frequency response analysis (SOL 111) leveraging the available solvers on the software Simcenter Nastran in order to show the analysis on a one-dimensional structure. The virtual point transformation method is analyzed and implemented starting from a simple two-dimensional structure such as a square plate, then it is applied to a three-dimensional structure such as an automotive rim, which represents a more significant case.

3.1 Modal analysis of a cantilever beam

This section has the main purpose of understanding the different implementations of Modal analysis. For all the cases it is considered a cantilever beam fixed on the left. The section of the beam is square, with the side of $h = 0.01m$, the material considered is steel with a young modulus of $E = 2.1 \cdot 10^{11} \frac{N}{m^2}$, a module density of $\rho = 7800 \frac{kg}{m^3}$ and a length of $L = 1m$. The analysis implemented are the Real eigenvalue analysis (SOL103), Modal frequency response analysis (SOL111) and Direct frequency response analysis (SOL108). The software Simcenter Nastran is leveraged to compute the modal displacements as well as the software Siemens Simcenter 3D to perform the animation and visualization of the displacements.

3.1.1 Dynamic analysis of a cantilever beam SOL 103

In this example it is applied the real eigenvalue analysis of a cantilever beam with a square section. The Real eigenvalue analysis is done leveraging the SOL103, which solve the equation of motion represented in equation 3.1: the solution of the equation of motion for natural frequencies and normal modes requires a special reduced form of the equation of motion 2.15, already depicted in section 2.2.2, which does not consider the damping and the load applied. With this solution the free vibration modes can be computed, which represent the modes of the structure without load applied to it.

$$[\mathbf{M}]\{\ddot{\mathbf{x}}(\mathbf{t})\} + [\mathbf{K}]\{\mathbf{x}(\mathbf{t})\} = \mathbf{0} \quad (3.1)$$

It is compared the plot of the modal displacements for three different modes between the extraction of the results from Matlab and the imported results on Simcenter 3D animated. The process to obtain the modal displacement is:

- Writing the solver .dat file automatically from a Matlab script, giving inputs to define the different cards leveraged from Simcenter Nastran.
- Solve the .dat file with the software Simcenter Nastran asking the modal displacement in the format of a .pch file
- The modal displacements are extracted from the .pch leveraging a Matlab script able to read the results and then plot them.

The card EIGRL is leveraged to select the Lanczos method to extract the eigenvalues in Nastran, in this case are asked the first 100 modes. It is considered the x axis as the axis on which the beam lay and the z axis as the vertical one.

Hereafter (figure 3.1) the plot of the results from Matlab for the **mode 2** at $8.38Hz$, **mode 5** at $147Hz$ and **mode 9** at $476.13Hz$ are reported.

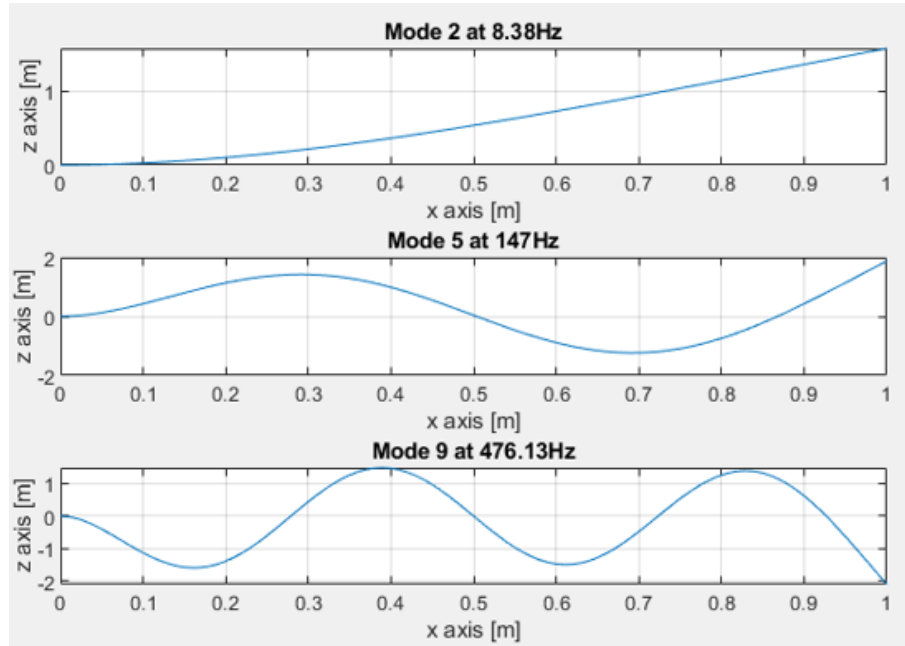


Figure 3.1: Cantilever beam, real eigenvalue analysis: Matlab plot mode 2, 5 and 9.

In figure 3.2 it is shown that the modes are perfectly reflecting the behavior consolidated from the animation on Simcenter 3D.

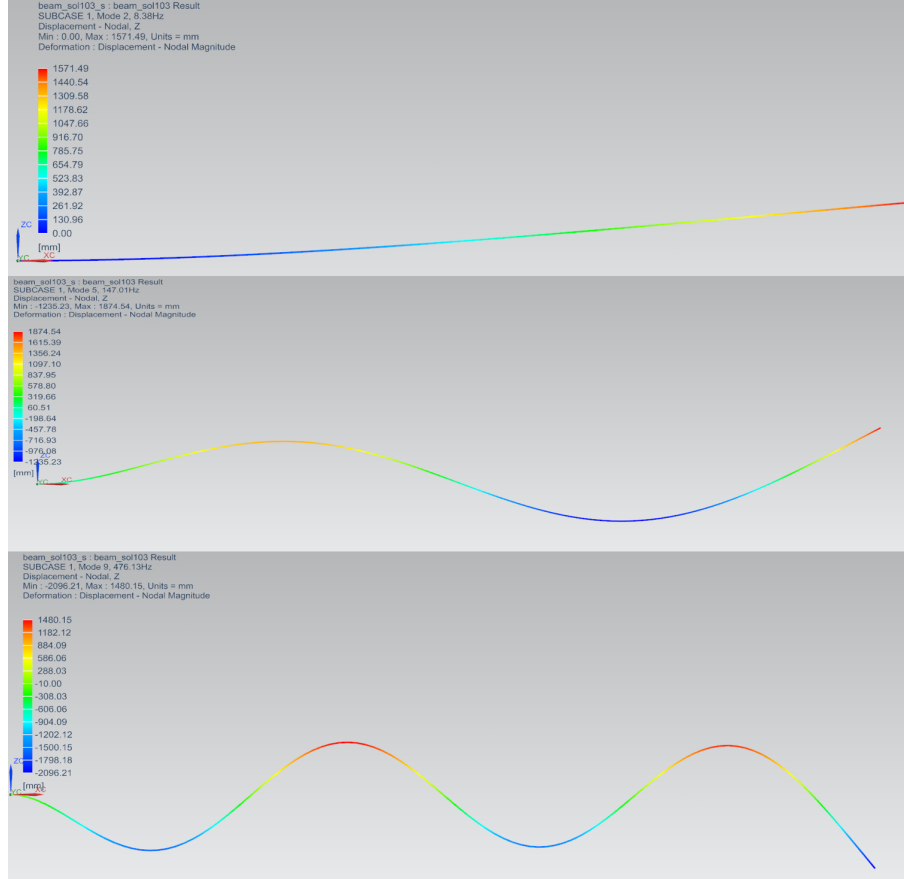


Figure 3.2: Cantilever beam, real eigenvalue analysis: animation of mode 2, 5 and 9 on Simcenter 3D.

3.1.2 Modal frequency response analysis: cantilever beam SOL 111

In this case a cantilever beam with a dynamic load, dependent on the frequency, and with unitary amplitude of 1N applied to the extreme right end is analyzed. The cards leveraged to define the dynamic load on Simcenter Nastran are **RLOAD1**, **DAREA**, **TABLED4**. The form of the dynamic load is depicted in equation 3.2.

$$\{P(f)\} = \{A[C(f) + iD(f)]e^{i\{\theta-2\pi\tau\}}\} \quad (3.2)$$

Where A is the amplitude of the load, $C(f)$ and $D(f)$ are respectively the real and imaginary part of the harmonic function, θ is the phase in degrees and τ is the time delay. With the card **FREQ1** we specify the range of frequencies for the dynamic load. In this case the range of frequencies is from $0Hz$ to $2048Hz$, from the solver nineteen modes are founded. In figure 3.3 it is showed the frequency response function in the specified range of frequencies highlighting the modes depicted in figure 3.1 and 3.2.

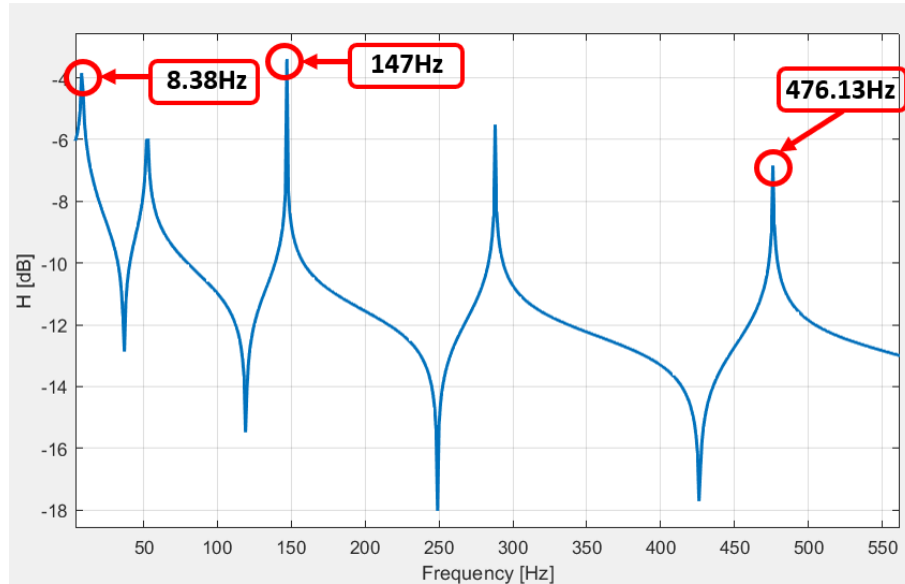


Figure 3.3: Cantilever beam, modal frequency response analysis: FRF from $0Hz$ to $2048Hz$.

It is evident that the SOL111 can come in help to identify the different modes of this one dimensional structure, they can be retrieved analyzing also its frequency response function.

3.1.3 Direct frequency response analysis of a cantilever beam (load at the end) SOL 108

In this case the cantilever beam with the same load conditions as in section 3.1.2 is considered. The SOL108 includes the direct frequency response analysis which is less computationally efficient with respect to the SOL111, since the SOL111 uses all the selected modes to solve the frequency response problem, whereas SOL 108 does a complex matrix solve at each requested frequency. We can see in figure 3.4 a comparison between the two analysis.

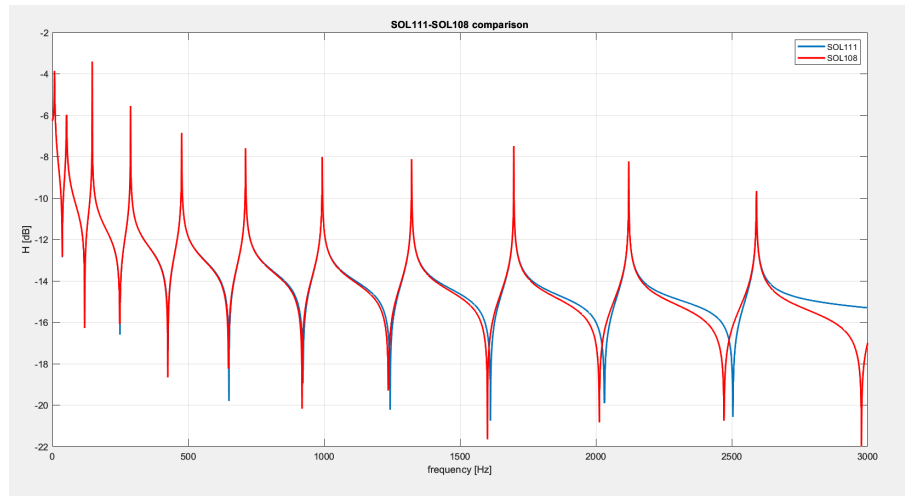


Figure 3.4: Cantilever beam, comparison SOL108 & SOL111 until 3000Hz.

Considering the plot in figure 3.4 the SOL108 compute the solution taking into account all the modes. Namely it can be noted on the extreme right in the response also a last antiresonance whereas the SOL111 do not show it, since it has neglected the contribution from the modes at higher frequencies that are not requested in the solution.

3.2 VPT application

The purpose of this section is introductory to the applications in simulation of the VPT, the focus is on the application and validation of the Virtual Point Transformation with two examples: one to validate the method on a square plate modelled in Simcenter Nastran and a more significant case of an Automotive Rim. The input dynamic load and the output accelerations are placed respectively in four points on the external surface.

3.2.1 Square plate

In order to show the implementation of the Virtual Point Transformation it is considered firstly a model of a square plate.

Properties of the square plate:

- Young modulus $E = 2.1 \cdot 10^{11} Pa$, the material chosen is steel
- Material density $\rho = 7.9278 \frac{kg}{m^3}$
- Poisson's ratio $\nu = 0.3$

- Thickness of the plate as $h = 0.01m$
- Side of the plate $L = 1m$

The plate is modeled and discretized on the software Simcenter Nastran implementing the CQUAD4 cards. The CQUAD4 card represents a quadrilateral plate element connection that connect on the edges of the element a number of 4 GRID cards, that are implemented to represent the nodes that discretize the plate. The size of each CQUAD4 is a square with a side of $0.01m$. The load applied is a dynamic unitary load of $1N$ of amplitude and the frequency range is $0Hz$ to $4000Hz$. In order to give a possible real picture that can be translated from CAE to a real testing environment, the input applied can simulate the application of shakers, and the output measured can simulate the usage of translational accelerometers. In this case the nodes where are applied the inputs are considered coincident with the nodes where are measured the output accelerations. The nodes where the forces are measured & applied are called as **indicators**. The coordinates of the indicators are showed in table 3.1. The x and y axis are considered laying on the plane of the plate and z as the vertical axis.

| | $x - coordinate[m]$ | $y - coordinate[m]$ | $z - coordinate[m]$ |
|---------------|---------------------|---------------------|---------------------|
| Indicator 1 | 0.18 | 0.26 | 0.0 |
| Indicator 2 | 0.24 | 0.8 | 0.0 |
| Indicator 3 | 0.72 | 0.22 | 0.0 |
| Indicator 4 | 0.76 | 0.72 | 0.0 |
| Virtual Point | 0.45 | 0.52 | 0.0 |

Table 3.1: Indicators and VP coordinates of the square plate case.

In order to gain an optimal implementation and results of the virtual point transformation it is assumed the hypothesis of rigidity, that is guaranteed from establishing a rigid connection between the nodes of the indicators and the virtual point. On the software Simcenter Nastran it can be implemented with the card RBE2: it establishes a rigid connection between two nodes implemented with the GRID cards. The formulation leveraged in this thesis for the VPT does not consider the contributes ensuing from the flexibility between the virtual point and the indicators, as a consequence this hypothesis comes in help to be compliant with the formulation. The model is represented in figure 3.5, where the RBE2 connections are highlighted with an orange line and the indicators with the three red arrows each, in order to specify the orientation of the axis for the input and the output.

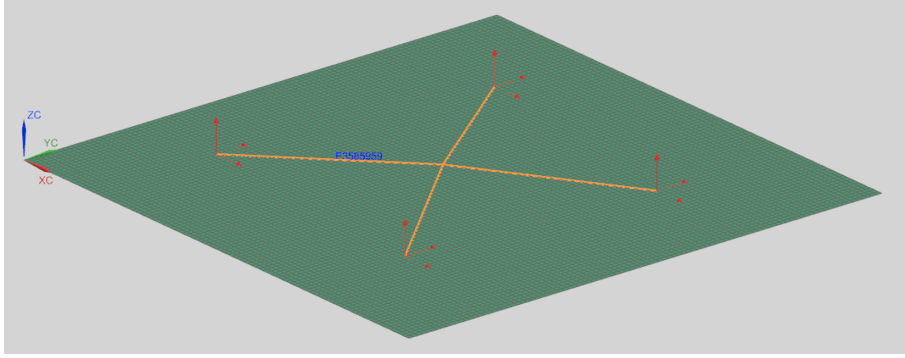


Figure 3.5: Square plate model on Simcenter 3D.

It is required in Simcenter Nastran to give as input three linear forces along the axis of the reference system for each indicator, as a consequence there are twelve different input forces. Then it is required also to gather data from four accelerometers on the indicators, in the end twelve accelerations in the range of frequencies are retrieved. With a Matlab script the results are read from the .pch file. Furthermore the FRF matrix $[H]$ of dimension (12,12) is composed, a different output corresponds to each row, whereas a different input corresponds to each column. In order to retrieve the FRF of the virtual point it is implemented the equation 3.3.

$$[\mathbf{H}_{VP}] = [\Psi_a]^+ \cdot [\mathbf{H}] \cdot [\Psi_f]^+ \quad (3.3)$$

Where $[H_{VP}]$ is the FRF matrix of the virtual point including the 6 DoFs, of dimension (6,6); $[\Psi_a]$ is the acceleration transformation matrix of dimension (12,6), the matrix is an extension along the rows from equation 3.4 in order to include all the four accelerometers.

$$[\Psi_a] = \begin{bmatrix} 1 & 0 & 0 & 0 & z_i & -y_i \\ 0 & 1 & 0 & -z_i & 0 & x_i \\ 0 & 0 & 1 & y_i & -x_i & 0 \end{bmatrix} \quad (3.4)$$

$[\Psi_f]$ is the force transformation matrix of dimension (6,12) and it is an extension along the columns of the equation 3.5.

$$[\Psi_f] = \begin{bmatrix} 1 & 0 & 0 \\ 0 & 1 & 0 \\ 0 & 0 & 1 \\ 0 & -z_i & y_i \\ z_i & 0 & -x_i \\ -y_i & x_i & 0 \end{bmatrix} \quad (3.5)$$

The index i represents the number of the indicator, in this case $i = 1,2,3,4$. In order to compare the results of the FRF of the virtual point, it is retrieved also the

FRF on the virtual point considering as indicator only the virtual point, allowing to compose directly the $[H_{VP}]$. It is showed in figure 3.6 the plot comparing the direct response and that one retrieved from the virtual point transformation. In this response we consider the linear force F_x as the input along the x - axis and the linear acceleration measured a_x as the output along the same axis.

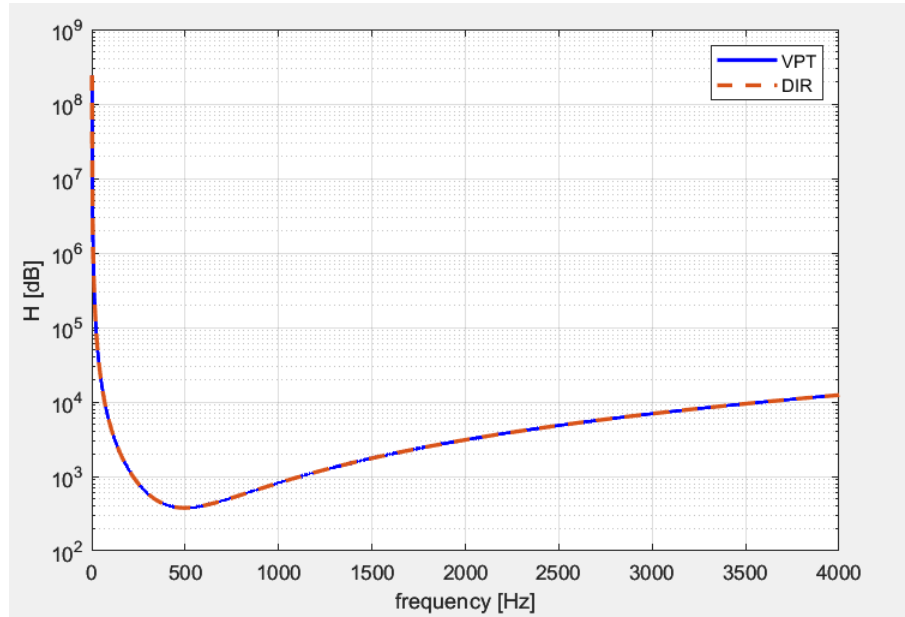


Figure 3.6: Comparison plot of the response of the virtual point along the x-axis.

From the plot it is shown that the responses match perfectly, the method has a good accuracy even at high frequency.

3.2.2 Automotive Rim

As a result it is proved that the virtual point transformation method has effective results on a 2D body, furthermore in this section it is applied the method also in a 3D model in order to prove the effectiveness also in more complex cases.

A model of an automotive rim is chosen, specifically has been retrieved a .stl file imported then on Simcenter 3D. The file contain a 3D model of a rim ensuing from a BMW 128 with the diameter of 18", as it is shown in figure 3.7.



Figure 3.7: 3D model of the BMW 128 rim.

In a real implementation the automotive rim has to be coupled with different kind of connections:

- Main hole connection to allow the coupling with the shaft.
- Five $M10$ holes for the connection through bolts between the rim and the hub.

In order to apply the FEA on the model on Simcenter 3D it is asked to the solver to compute the .DAT file modeling the mesh of the body with tetrahedral elements including four grid points each, with the size of the element of $1mm$. The implementation of the four sided isoparametric solid element is obtained through the card **CTETRA**. The material chosen is the aluminium alloy 2014, that is among the materials that shows the best performances for this automotive component [39]. The modulus of elasticity of the material is $E = 7.35 \cdot 10^{10} MPa$, the poisson's ratio is $\nu = 0.33$ and the density is $\rho = 2.685 \frac{g}{cm^3}$. The whole model is showed in figure 3.8.

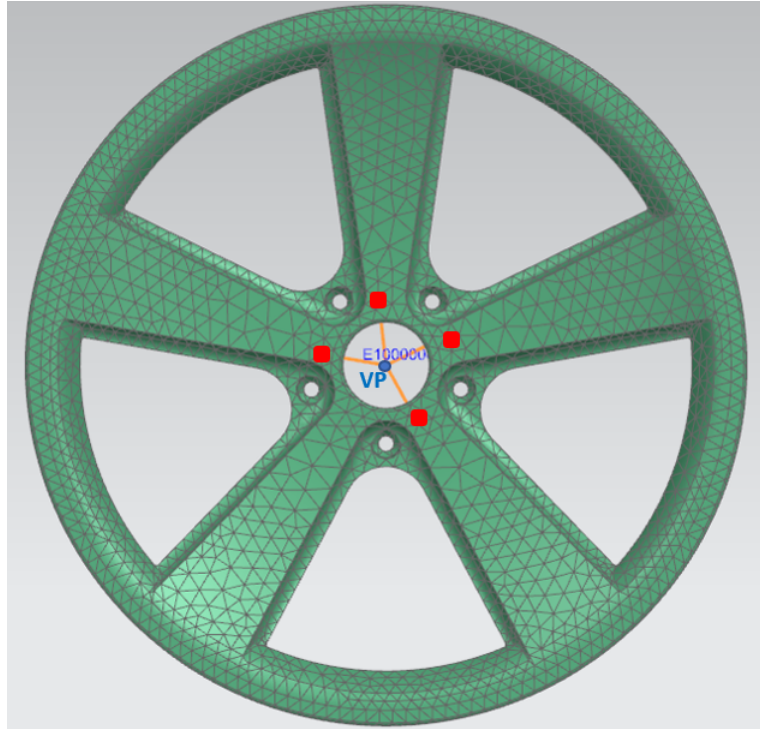


Figure 3.8: Tetrahedral mesh of the BMW 128 rim.

As it can be noted the virtual point chosen is in a non-physical point, in the middle of the main hole. In order to obtain a rigid connection between the indicators (highlighted with red squares in the picture) one RBE2 card is implemented, connecting the virtual point with the four GRIDs that locate the indicators. In table 3.2 the coordinates of the virtual point and the indicators are showed. Also in this case the indicators comprise the location of the input that is

| | $x - coordinate[m]$ | $y - coordinate[m]$ | $z - coordinate[m]$ |
|---------------|---------------------|---------------------|---------------------|
| Indicator 1 | -0.037072 | -0.067258 | 0.015977 |
| Indicator 2 | -0.020597 | -0.067255 | -0.03561 |
| Indicator 3 | 0.027585 | -0.067252 | -0.03183 |
| Indicator 4 | 0.76 | 0.72 | 0.0 |
| Virtual Point | 0.0 | 0.01 | 0.0 |

Table 3.2: Indicators and VP coordinates of the automotive rim case.

coincident with the location of the respective output. We can see that the virtual point transformation method works properly in this case, as a result it is reported in figure 3.9 the plot of the response with linear input F_y along the $y - axis$ and

as output the linear acceleration a_x along the x – axis. We can see that the direct response measured on the virtual point and the response obtained applying the method are perfectly matching even in a high frequency level as $4000Hz$.

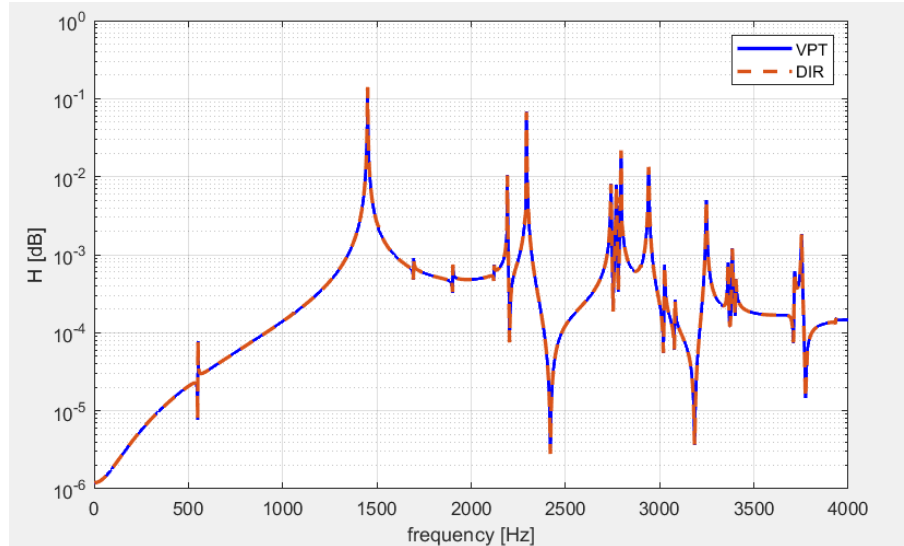


Figure 3.9: Response of the automotive rim with direct and response applying vpt, F_y as input and a_x as output.

To summarize different considerations can be done:

- In order to analyze the dynamic behavior of a body different kind of analysis can be conducted. In CAE the software Simcenter 3D and Simcenter Nastran represents useful tools to implement the Real eigenvalue analysis, the Modal frequency response analysis and the Direct frequency response analysis through the various solvers available on the software.
- A useful approach to gain an overall awareness of the dynamic behavior of a body is to retrieve the animated representation of the modes of the structure (as in Simcenter 3D with the SOL103) plus retrieving the FRF of the structure.
- The differences in terms of quality and computational cost between the SOL108 and the SOL111 are highlighted, leading to consider in a careful way which kind of analysis, between the Direct frequency response analysis and the Modal frequency response analysis, to use.

- The virtual point transformation is a theoretical method that can be implemented and validated leveraging different simulation tools. Firstly modeling the body (that can be a 2D or a 3D structure) with FEM through the software Simcenter 3D, then solving the specific analysis with the software Simcenter Nastran and finally postprocessing the results with Matlab implementing the theoretical formulation of the VPT.

Chapter 4

Experimental Issues of VPT in CAE

The goal of this chapter is to analyze on CAE the possible errors that can ensue on setting-up the test bench for the experiments on an automotive rim and how they influence the accuracy of VPT. Indeed in the physical implementations the location where the shaker (input) and the accelerometers (output) are applied cannot coincide, and from this mismatch some errors in the VPT can ensue. Furthermore it is showed the importance of the rigidity hypothesis for the method and how it can be useful to avoid errors ensuing from flexibility.

4.1 Experimental issues in real testing environment

In a real testing environment for NVH purposes the positioning of the tools leveraged for measure and excite the structure to test are crucial. The first step to follow is to choose the location on which apply the tools. The virtual point transformation method is strictly dependent from the location of the input load and the measurement sensors. The notation used in the next sections is briefly depicted:

- **Input:** as discussed in the previous chapters the input load is implemented through a shaker. The input is the location in which the shaker is implemented.
- **Output:** in order to gather data the output measured is the acceleration. The output represents the location in which the accelerometer sensor is applied.
- **Indicator:** the indicator is the general notation that consider both the input shaker and the output accelerometer sensor.

As shown in figure 4.1, usually for NVH test that are done on an automotive rim the configuration consist in implementing the accelerometer sensor fixed on the shaker.



Figure 4.1: NVH test on an automotive rim: location of the indicators.

The sides on which in a testing environment the user can have freedom are represented from the choice of the relative distance between the accelerometer and the shaker and the positioning of the overall indicators on the body to test with

respect to the virtual point. It is still a case of study which configuration can lead to the best results, considering the location of the indicators with respect to the virtual point as well as where to locate the indicators avoiding regions with more flexibility. Another challenge is represented from the choice of the dimension of the block that represents the indicator: namely the size can be modified changing the distance between the accelerometer and the shaker. In section 4.3.3 there is an attempt to represent the physical blocks.

4.2 Sensitivity analysis

In this section are analyzed through simulation the possible dependencies of the VPT from flexibility. In the first case it is demonstrated how the hypothesis of rigidity is fundamental to ensure the validity of the method whenever is applied without considering the contribution of the nonlinearities ensuing from the flexibility in the formulations. The latter case has as a main purpose to prove that the distance of the indicators from the virtual point has a considerable influence on the quality of the results. Both the cases give an overview of how the method can be sensitive in the setup of the test benches and if are not applied the right hypothesis.

4.2.1 Rigid connection VP-center hole/VP-indicators and comparison

The body on which the method is implemented is the automotive rim component of a BMW 128 car, shown in section 3.4.2. The properties of the material are the same, as well as the loads and locations of the indicators. The virtual point is still a non-physical point that is represented on Simcenter 3D as a node with the GRID card; it is located on the center of the main center hole of the rim, and it is laying on the same plane of the interface side of the rim that can be coupled with the hub component. Hereafter the two cases of rigidity are shown, in which the virtual point is fixed in two different ways. The indicators location is represented with red squares, the rigid connections are represented with yellow lines, whereas the area of rigidity is highlighted with a blue area (Figure 4.2).

- **Rigid connection between virtual point and indicators:** in this case the hypothesis of rigidity is perfectly satisfied. This happens because **RBE2** card impose a rigid connection between the virtual point and the indicators, so there are four rigid connections as shown in figure 4.2.

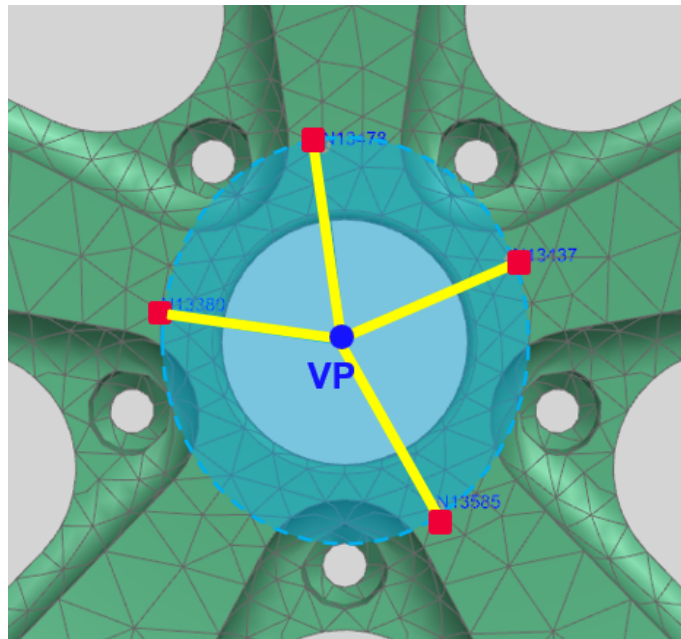


Figure 4.2: Area of connection of the automotive rim: VP-Indicators.

The distribution of the rigid connections can be seen more clear in figure 4.3 without the FEM model.

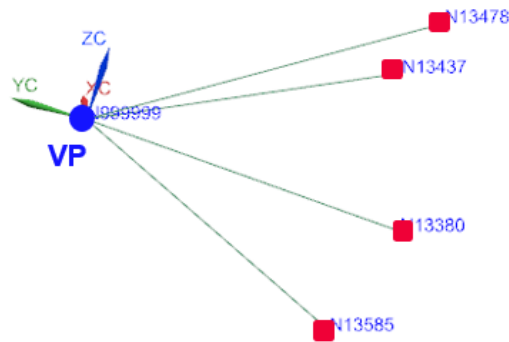


Figure 4.3: RBE2 connections between the virtual point and the indicators.

It is shown then in figure 4.4 the linear response, that consider $a_x - a_y - a_z$, from the linear inputs $F_x - F_y - F_z$. On the same plot the response obtained applying the VPT and the response measured directly on the virtual point node are compared.

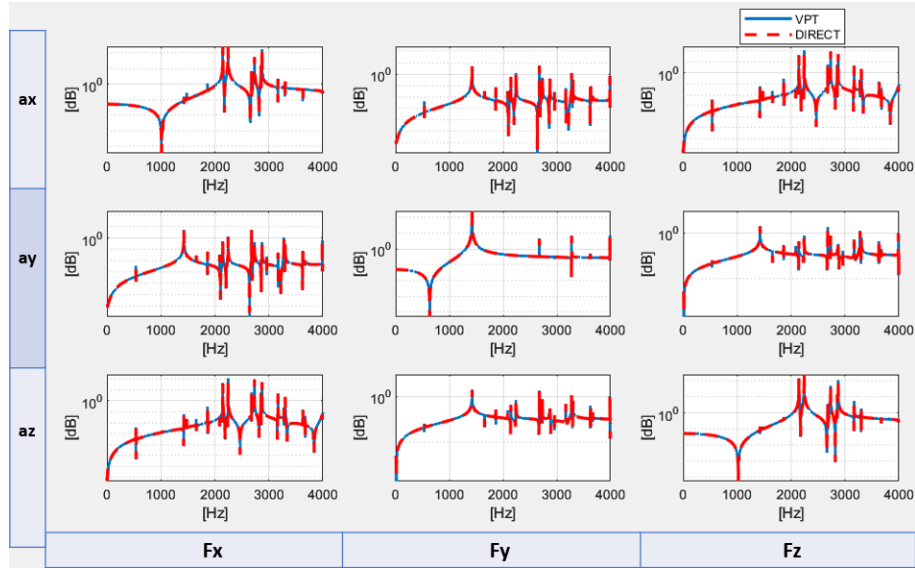


Figure 4.4: Plot of the linear response of the case with hypothesis of rigidity.

It is proved that the virtual point transformation method works properly with the hypothesis of rigidity.

- **Rigid connection between virtual point and the center hole surface:** in this case a rigid connection between the virtual point and three points laying on the internal surface of the main center hole of connection has been established. There are only three rigid connections with nodes that are different from the indicators locations. There is no rigid connection between the virtual point and the indicators, furthermore the rigidity is noticeably reduced, leading to poorer results. As showed in figure 4.5 also the area of rigidity is reduced with respect to the previous case.

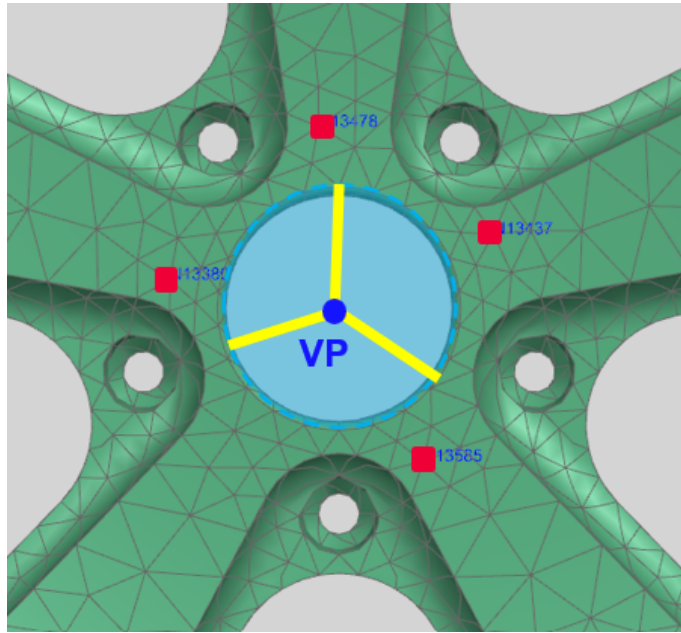


Figure 4.5: Area of connection of the automotive rim: VP-Center hole.

In figure 4.6 the rigid connections and the plane of interface aimed at creating a contact between the rim and the hub are shown.

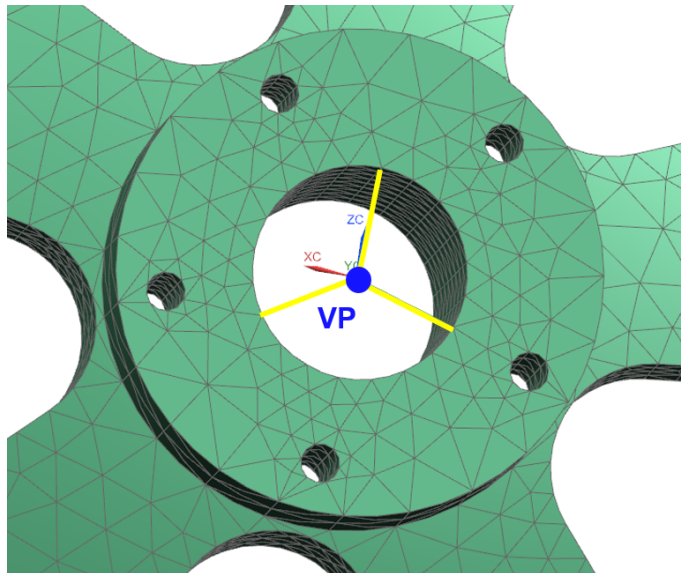


Figure 4.6: Back side of the rim, plane of the RBE2 connections and the virtual point.

Without the hypothesis of rigidity the method is likely to worsen even starting from low frequencies, as it is shown in figure 4.7 and 4.8. There is an evident discrepancy between the direct response and the response implementing the VPT.

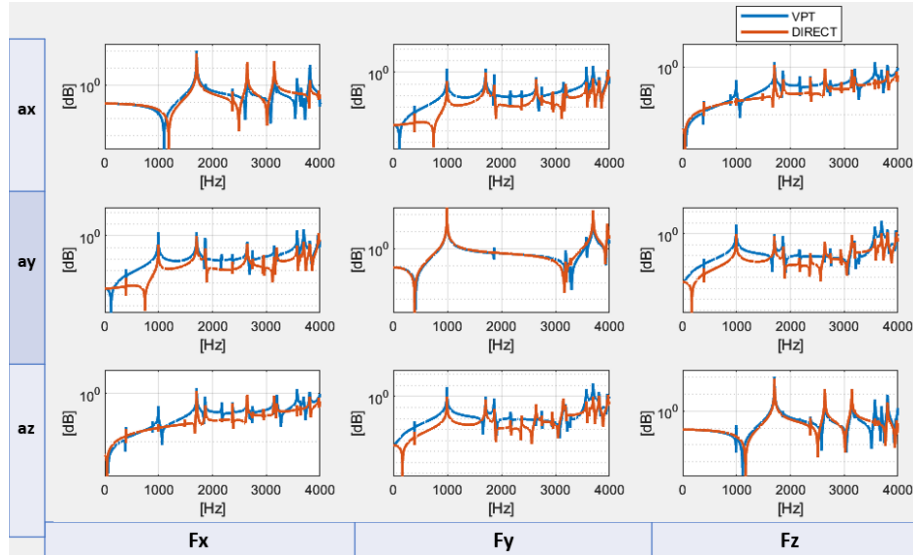


Figure 4.7: Plot of the linear response of the case without hypothesis of rigidity.

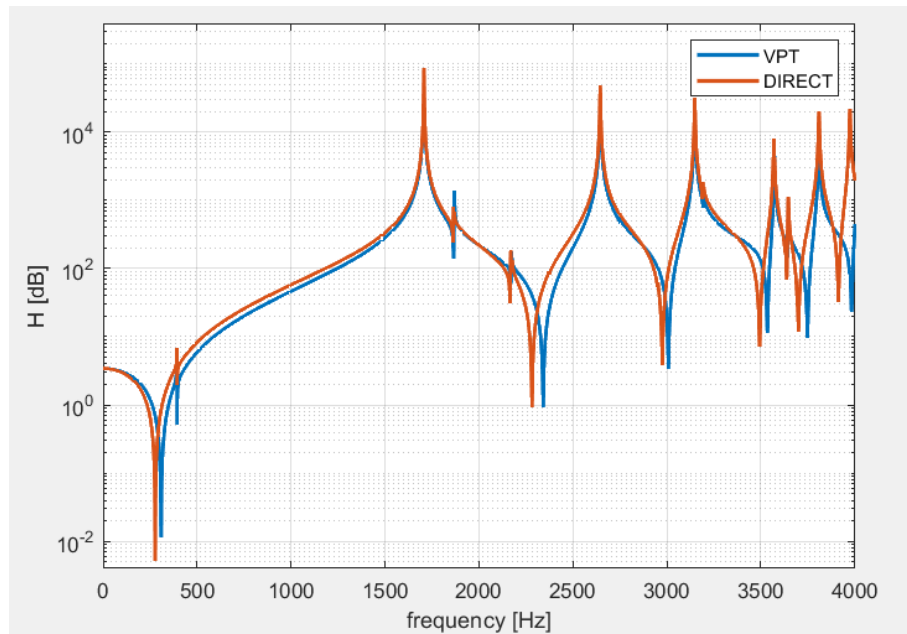


Figure 4.8: Virtual point transformation: no rigidity hypothesis.

In figure 4.8 it is shown a response from the figure 4.7, it is relative to F_y as input and a_x as output. A difference between the two responses compared can be noted starting from the range of $100Hz$.

4.2.2 Influence of the distance of the indicators on the accuracy of VPT

In this section it is analyzed how changing the distance of the indicators with respect to the virtual point can have impact on the results. There is a focus also on the importance of the flexibility of the whole structure and how important can be the choice of the location of the indicators. It is shown that doing a prior real eigenvalue analysis and analyzing the free mode shapes of the structure to test in simulation can contribute to choose the right location of the indicators. The case without rigidity hypothesis is chosen: there are three rigid connections with RBE2 card connecting the virtual point and three points inside the main center hole of connection, laying on the plane of contact for coupling the rim with the hub component. As it is shown in figure 4.9 two different distances are chosen, one closer to the virtual point, highlighted in light blue, and one far on the radius of the wheel, highlighted in light green.

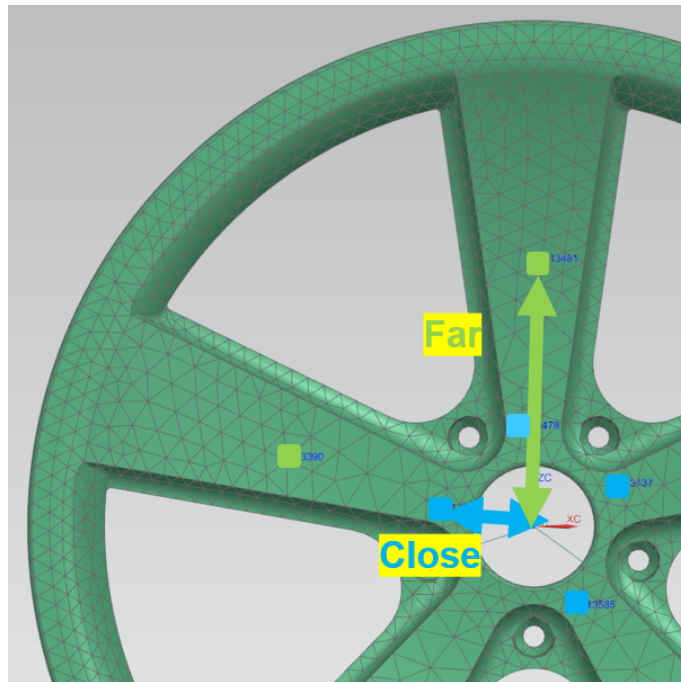


Figure 4.9: Positioning of the indicators in two distances.

Firstly the results of the application of the virtual point transformation with a response from the input F_x and the output a_x are compared, as shown in figure 4.10.

There is also a comparison between the response of the far and close indicators with the reference response measured directly on the virtual point. The frequencies analyzed are from $0Hz$ to $4000Hz$.

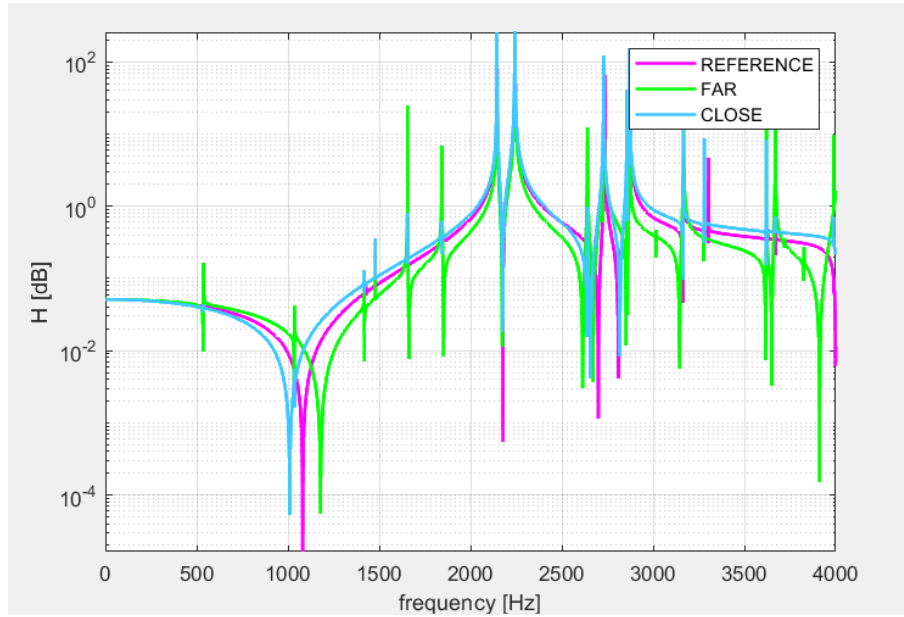


Figure 4.10: Response comparing reference, close and far indicators. Input F_x and output a_x .

Relevant discrepancies between the response of the closer indicators and the far indicators in specific modes with the mode shapes highlighted in animation with the software Simcenter 3D are correlated, it can be noted that at the natural frequencies the structure flexibility play an high role on the positioning of the indicators. In the count of classification number of the mode also the first four rigid body modes, that represent the first four modes of the structure are considered.

Relevant mode shapes:

- **Mode 8** at 535Hz . The response and the mode shape animated are shown in figure 4.11 and 4.12.

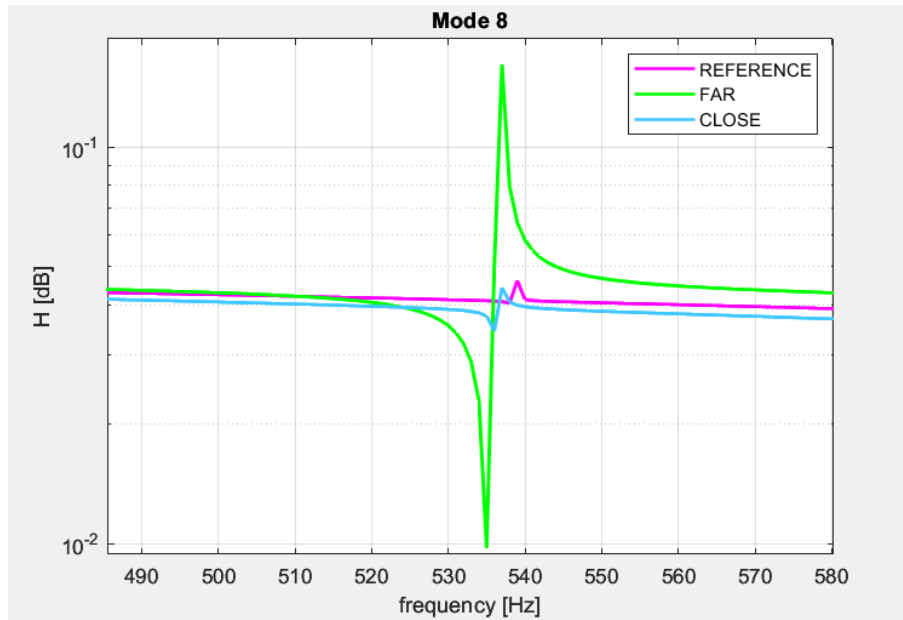


Figure 4.11: Mode shape 8 at 535Hz

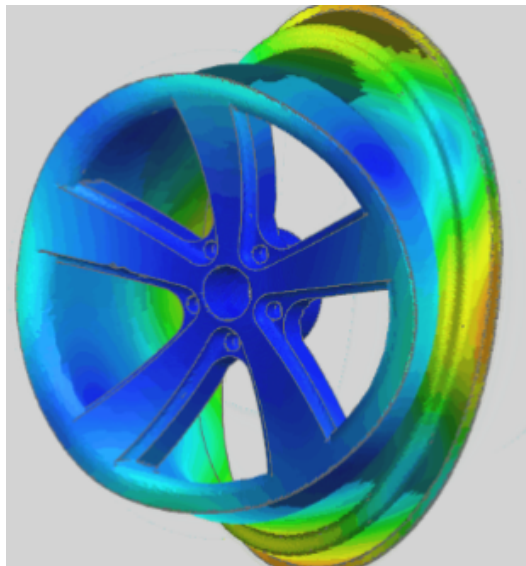


Figure 4.12: Animation of the eight mode shape

It can be noted that at this frequency the radius of the rim are warping along the $x - axis$, furthermore that moving along the radius the deformation is more evident.

- **Mode 11, 12 & 13.** In figure 4.13 the three mode shapes that show in simulation the more critical deformations along the $x - axis$ are shown.

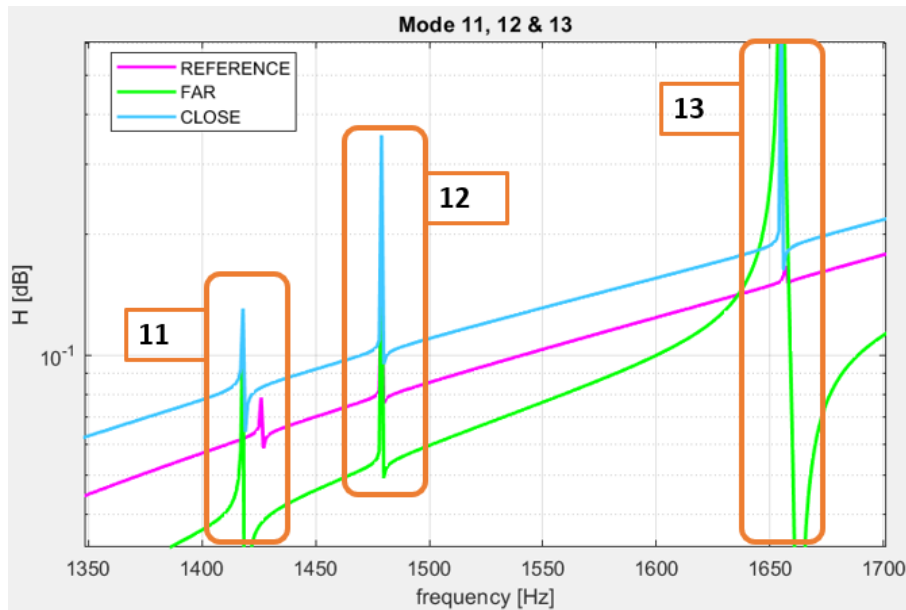


Figure 4.13: Mode shapes 11, 12 & 13

The animations of the respective modes are showed in figure 4.14.

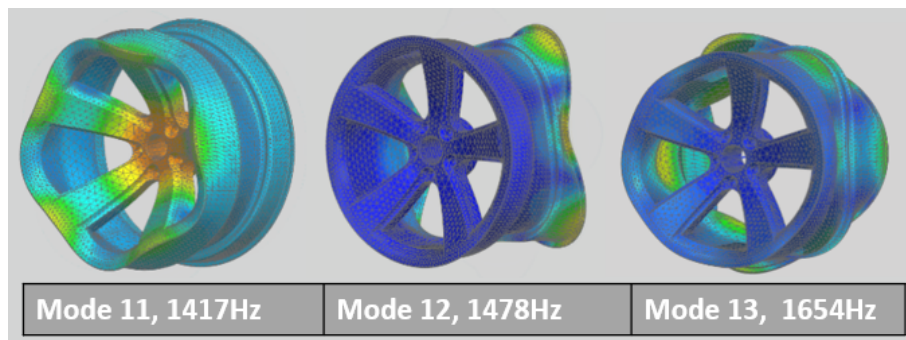


Figure 4.14: Mode shapes 11, 12 & 13

As a result the higher amplitude of mode 13 is perfectly expressed on the animation, where the deformation along the $x - axis$ has a noticeable

entity. Whereas for mode 11 & 12 it can be noted that the amplitude of the mode shapes is higher for the closer indicators, namely on the animation the displacement is more relevant close to the center of the connection.

4.3 Environmental Error analysis

In this section there is an analysis and an attempt to reproduce the possible errors called "environmental errors" that can ensue from a bad set up preparation in the test phase, for situations in which there is the need to apply the virtual point transformation method. The analysis is focused on the influence and the impact that various kind of errors can have on the quality of this method.

4.3.1 Output moved radially along the Rim

In this section it is considered a case in which the set of four indicators are moved gradually far from the virtual point (figure 4.15). The purpose is to understand how the decreasing accuracy and the overall quality reduction of the virtual point transformation can be represented. If the indicators are moved, these are placed radially along the rim.

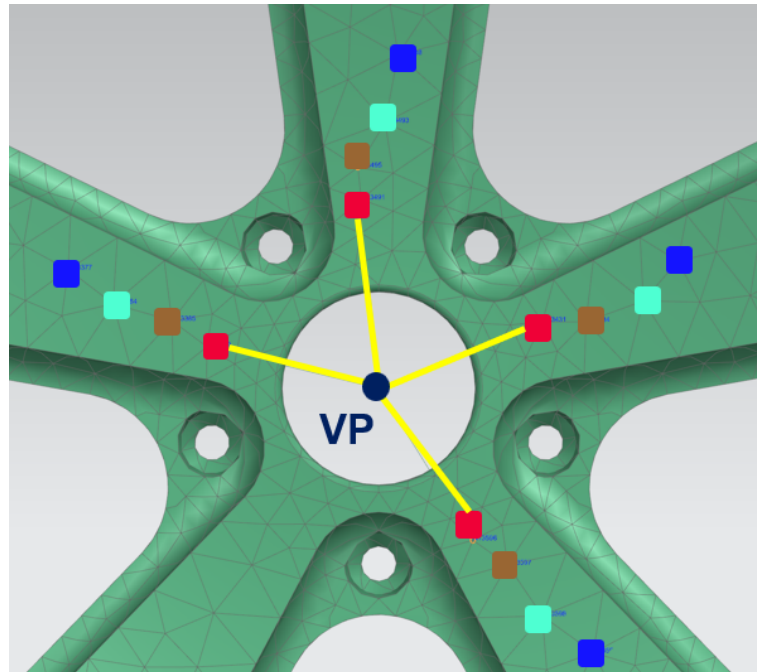


Figure 4.15: Case: indicators moved along the radius of the automotive rim.

Assumptions:

- The **input forces locations** remain in the first set of nodes highlighted in red.
- The **output accelerometers locations** change from the red to the blue position as shown in figure 4.15. Only in the first case, highlighted in red, the location of the input and the output are coincident.
- The transformation matrices $[\Psi_a]$ and $[\Psi_f]$ are constant. So doing, the geometrical informations in the formulation are kept as the original. Every deviation will be included only in the dynamic response H_{ij} , as happening in the experimental case.
- The set of nodes in red act as a reference. In this case all the requirements for implementing in the proper way the virtual point transformation are satisfied resulting in a perfect accuracy.
- In all the cases there are four rigid connections implemented with RBE2 cards, connecting the virtual point and the location of the input (red set of nodes).

Hereafter there is a comparison between the four cases involving the frequency response. There are two main results and observations that can be highlighted:

1. One consequence of this kind of error is the decrease of accuracy in the method, specifically can be noted that the distance of the indicators from the virtual point is proportional to the error ensuing on the frequency response function. In figure 4.16 the responses with F_z as input and a_z as output are considered. It is highlighted that the more the distance increase, the larger the difference with the reference response become.

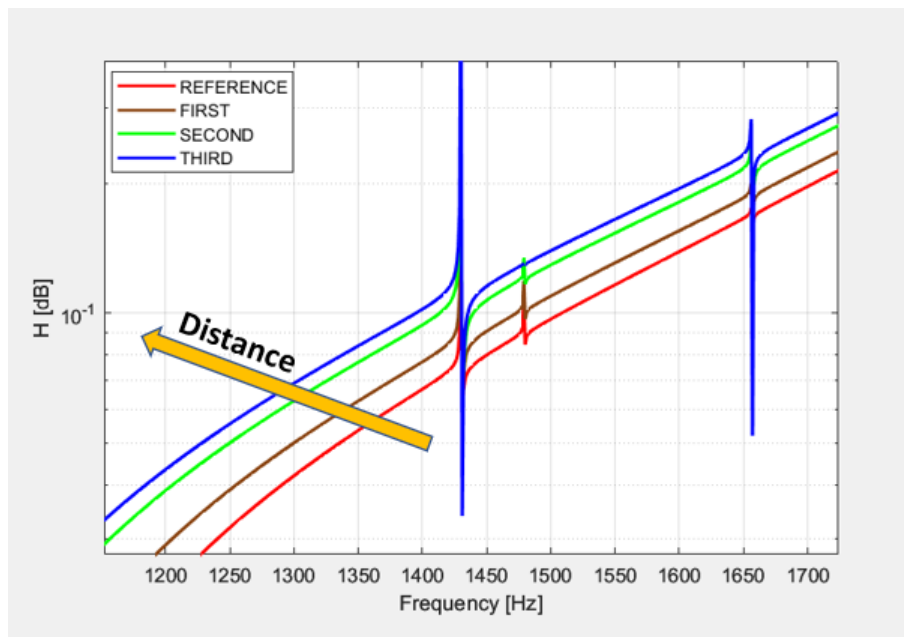


Figure 4.16: Response along $z - axis$ with linear input and output.

2. In figure 4.17 it is showed that changing the distances determine also the loss in the symmetry in the obtained FRF. This can ensue from the loss of the rigidity hypothesis in all the other cases except the reference case.

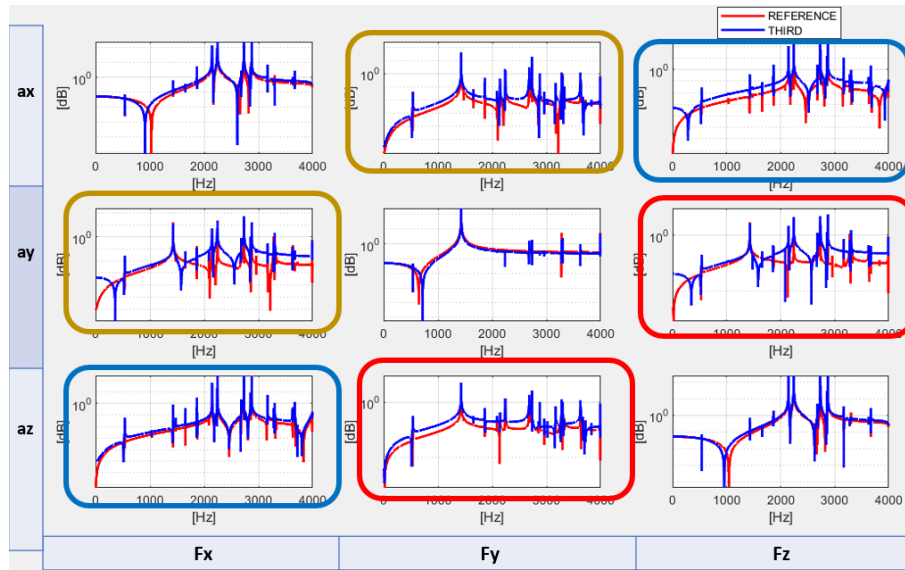


Figure 4.17: FRF linear responses and output: Loss of the symmetry.

It is reported only the linear and output responses along the three main axis of the reference case and the third distance.

4.3.2 Output moved around the input - Close and Far distances

The purpose of this section is to reproduce the environmental error, specifically in testing environment it is not possible to locate in the exact same position the accelerometers and the shakers that will impose the load on the structure, namely there will be always a discrepancy between the positioning of the input and the output indicators. The main aim is to analyze how this kind of error can be reflected on the quality of the virtual point transformation method. Five different sets of locations in two cases are considered: one located close to the virtual point and one located far on the radius of the rim. The distribution of the sets is around the reference set, of which the location of the indicators is highlighted in red.

Assumptions:

- The red set acts as a reference, as a matter of fact the location of the input and the output coincide in the same node.
- Three rigid connections are established between the virtual point and three nodes chosen on the internal surface of the main center hole of connection, laying close to the plane on the back side of the rim aimed for the coupling with the hub. Three RBE2 cards are leveraged.

- In all the cases and sets the input is located in the reference set highlighted in red.
- In the distribution around the reference, the distance between the reference node and the four sets on which the input is switched is $1cm$.
- In both the two cases the location of the output accelerometers is moved on the four sets of nodes with respect to the reference: the black set is moved radially toward the virtual point; the blue set is moved far from the virtual point radially with respect to the reference; the green set is moved leftward with respect to the reference; the brown set is moved rightward with respect to the reference.

Cases analyzed:

1. Output moved around the reference: Close distance

In this case the output location that reproduce a real implementation of an accelerometer is moved around the reference set, the whole distribution is located close to the virtual point, near the main center hole of connection of the rim, as it is shown in figure 4.18.

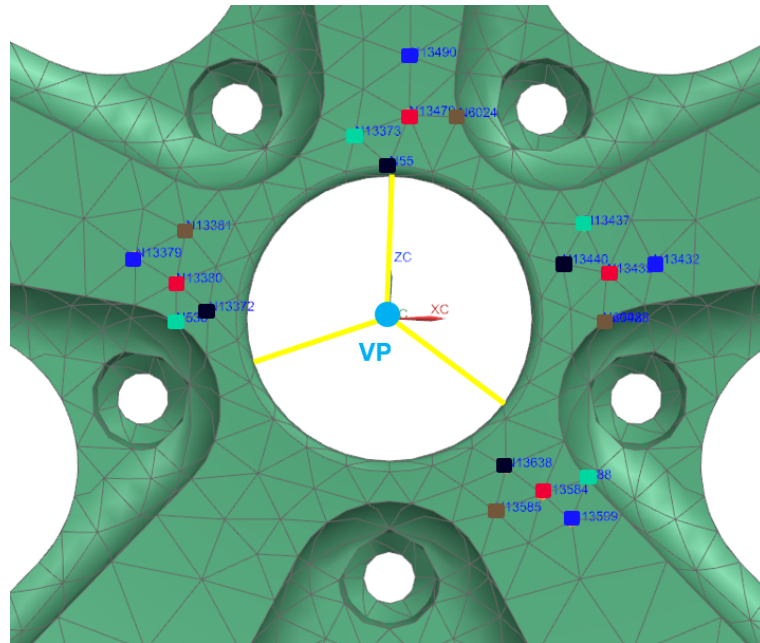


Figure 4.18: Distribution of the input output locations of five set of nodes, close to the virtual point.

The only response that has good results is the one considering the input as F_y and as output a_y as we can see in figure 4.19.

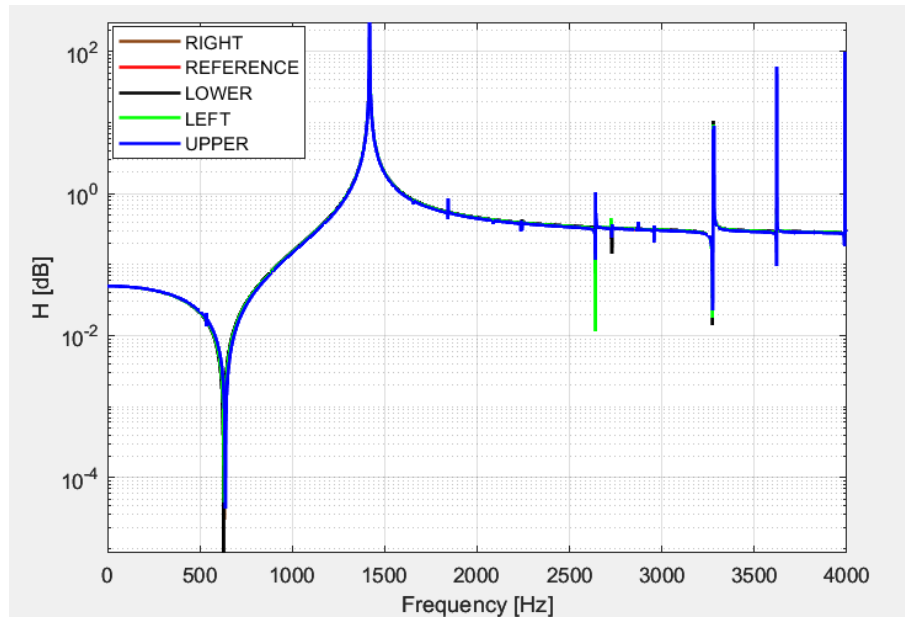


Figure 4.19: Response on F_y as input and a_y as output.

It can be noted also that positioning the output on the right and left locations the responses stay more closer to the reference whereas the upper and lower locations show a larger difference with respect to it. This is caused by the higher flexibility on the radial direction. The acceptable results on this response can be caused from the lower flexibility of the rim on the axial direction if it is solicited along it. The higher error on the locations switched radially on the radius is also present in the responses with input F_x and output a_x , as well as in that one with input F_z and output a_z .

2. Output moved around the reference: Far distance

Hereafter it is analyzed the case with the same formation of the locations, the input and output moved in a region more far from the previous case following the radial direction, along the radius of the rim. The distribution of the indicators is shown in figure 4.20.

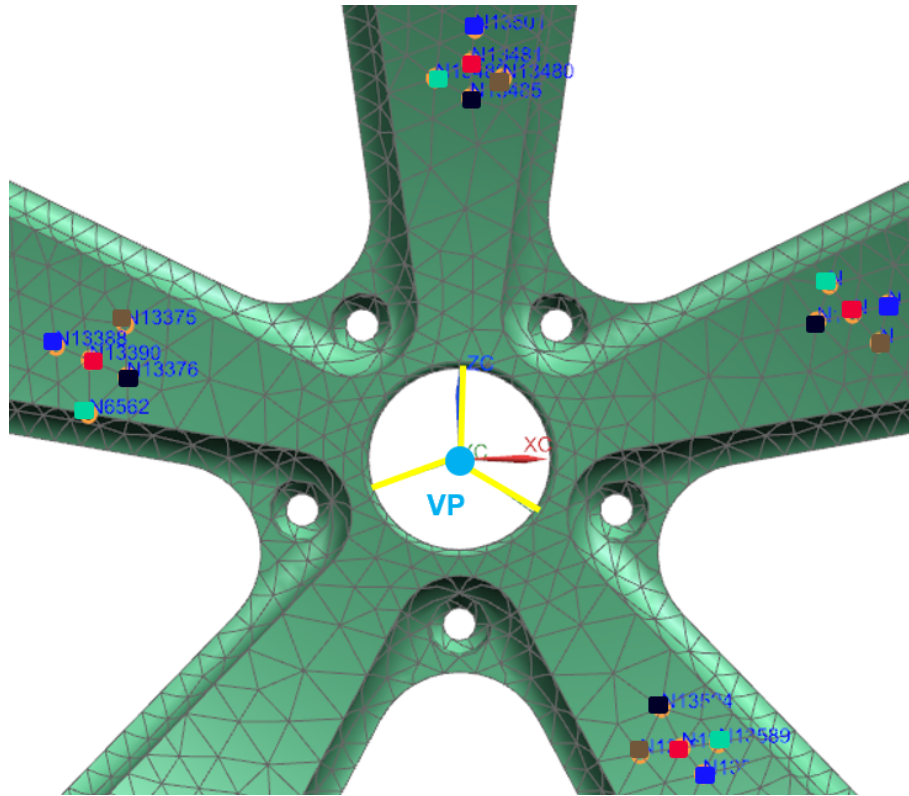


Figure 4.20: Distribution of the input and output locations of five set of nodes, far from the virtual point.

The responses in which the method has better results are that ones where the direction of the input load and the output measured are the same. The response with the input as F_y and the output as a_y is reported in figure 4.21.

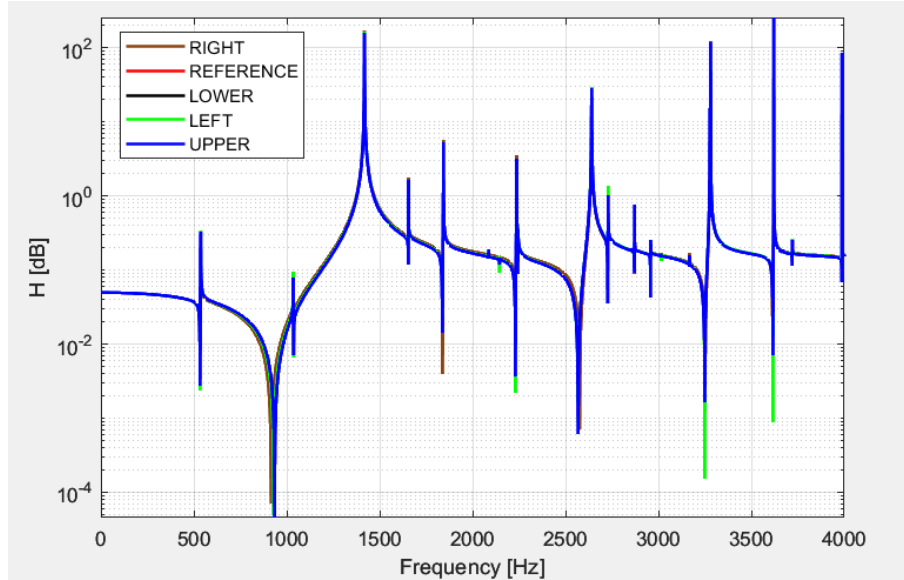


Figure 4.21: Response with input F_y and output a_y .

A perfect match in these cases can be highlighted between the response of the reference and the upper as well as the lower locations. Whereas we can see that the responses of the right and left locations cannot reproduce the same results of the reference. This ensue from the fact that the flexibility of the radius is more homogeneous on the radial direction when we work on the region where we are not close to the center hole neither the external surface of the rim. Overall we can assume that this kind of environmental error has less entity on a region where the difference of rigidity with the surrounding regions is negligible, so in an area where the flexibility is homogeneous.

4.3.3 Reproduction of Indicators as sensors and validation of reciprocity

The aim of this section is to apply the virtual point transformation method in a real case in which the input shaker location and the output accelerometer location are overlapped, namely we try to reproduce two cases: one in which we apply the accelerometer on the body, and then the shaker on top of it and the second one implementing firstly the shaker and then on top the accelerometer. We will do also a comparison between the two cases in order also to see how they will influence the

overall quality of the outcome from the method applied.

Assumptions:

- For all the cases the range of frequencies analyzed it is from $0Hz$ to $2000Hz$.
- Four RBE2 cards are exploited with the aim to represent the indicators. The indicators in all the cases represents the bodies that comprise the accelerometer and the shaker (figure 4.22). The black nodes represent the possible location of the input and the output.

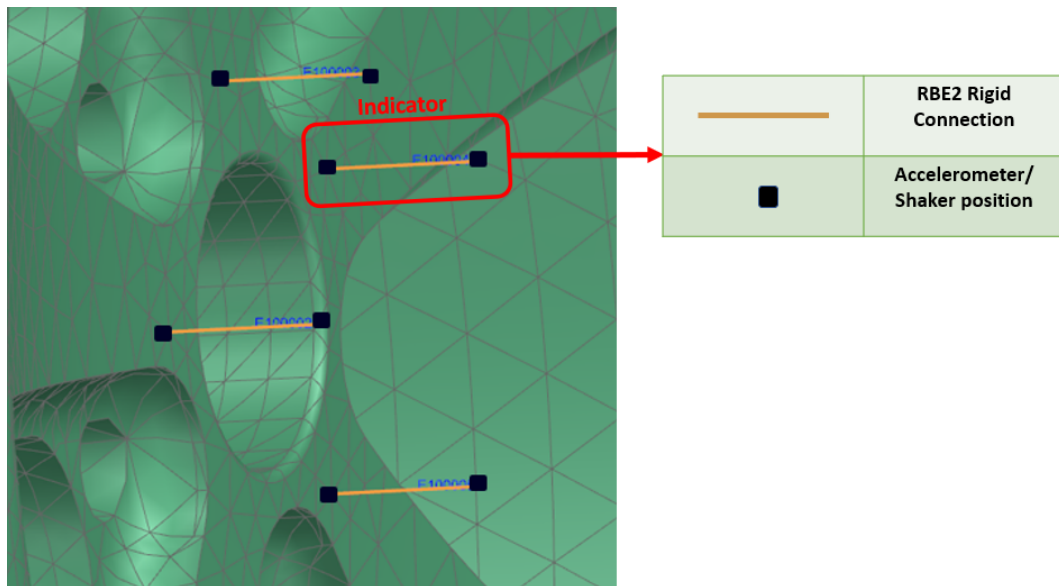


Figure 4.22: Indicators location and structure.

- For all the cases three RBE2 cards are leveraged in order to establish the rigid connections between the virtual point and three nodes on the internal surface of the main center hole. In picture 4.23 the overall distribution of the rigid connections is highlighted from a perspective of the lateral side of the model.

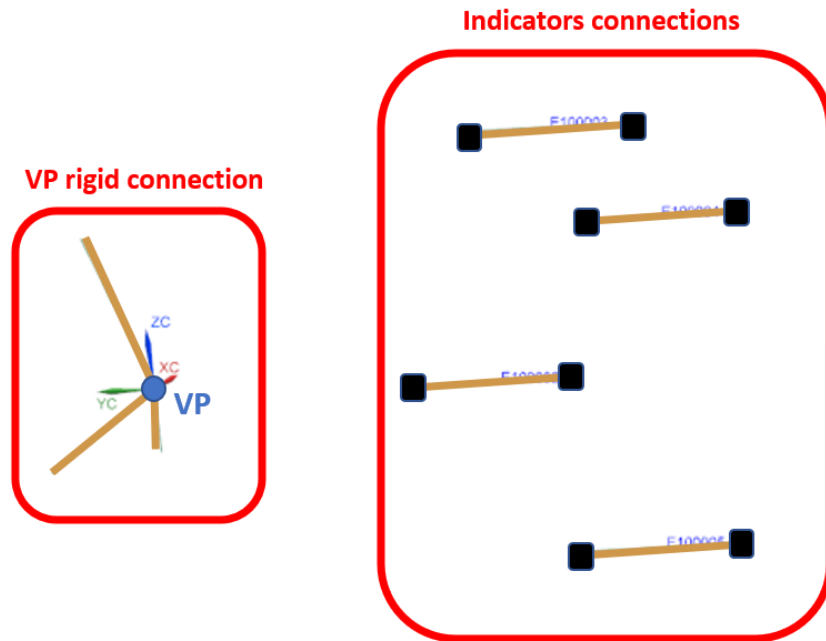


Figure 4.23: RBE2 distribution: on the left the connections with the virtual point (VP), on the right that ones representing the indicators.

- In all the cases the coordinates of the nodes implemented to build the transformation matrices Ψ_a and Ψ_f are that one of the nodes that touch the surface of the rim.

1. **Accelerometer on the surface, shaker on top:** In this case the accelerometer that measures the output accelerations on the surface of contact with the automotive rim (highlighted in red) is implemented, whereas the input shaker location is implemented externally on top of it (which is highlighted in black), as shown in picture 4.24.

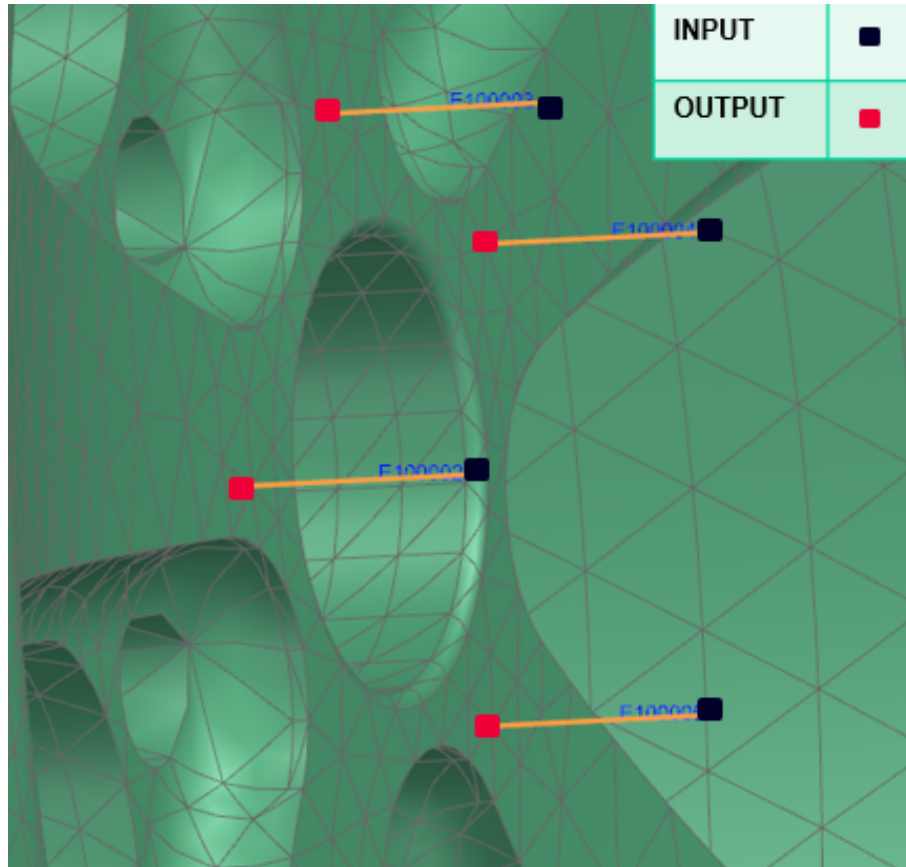


Figure 4.24: First case reproducing sensors, output in the surface of contact and input on top.

In order to measure the results hereafter the plot of the responses considering only linear input loads and linear output measurements are reported in picture 4.25.

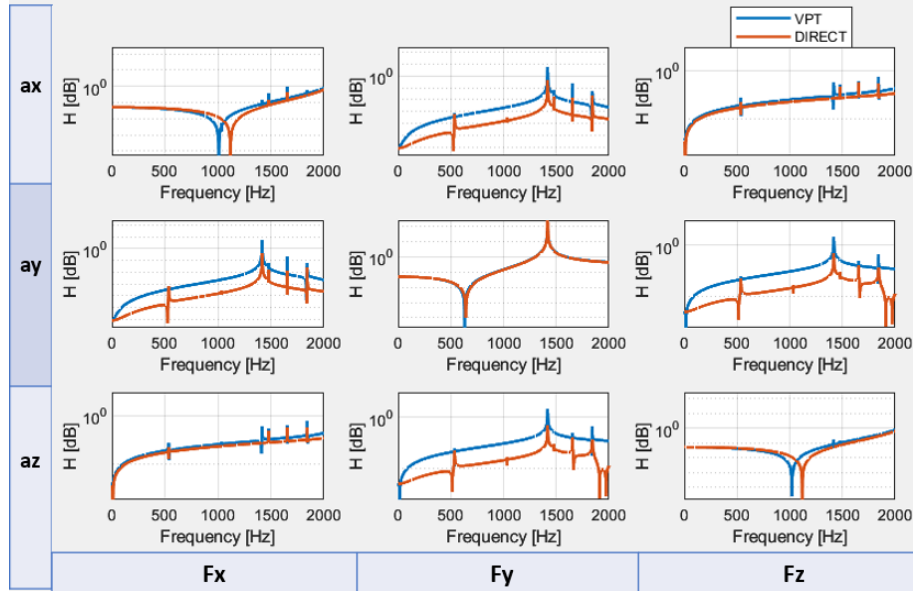


Figure 4.25: First case plot of the responses considering only linear inputs and outputs.

It has to be considered that the hypothesis of rigidity is not respected since the rigid connections between the virtual point and the indicators are not implemented. As a consequence a discrepancy between the compared responses is expected. It can be noted that the response from the method and the direct response from the virtual point match until 500Hz only on the responses in which the input and the output lays on the same axis. Whereas the best accuracy in the wider range of frequency is obtained only in the response with input and output coincident on the $y - axis$. These results can ensue from the fact that along the $y - axis$ the direction of the loads and outputs pass through the body so the structure is more rigid and compact.

2. **Shaker on the surface, accelerometer on top:** In this case the accelerometer is placed on top of the shaker so on the external extreme of the rigid connection, whereas the shaker is implemented on the surface of the body as we can see in picture 4.26.

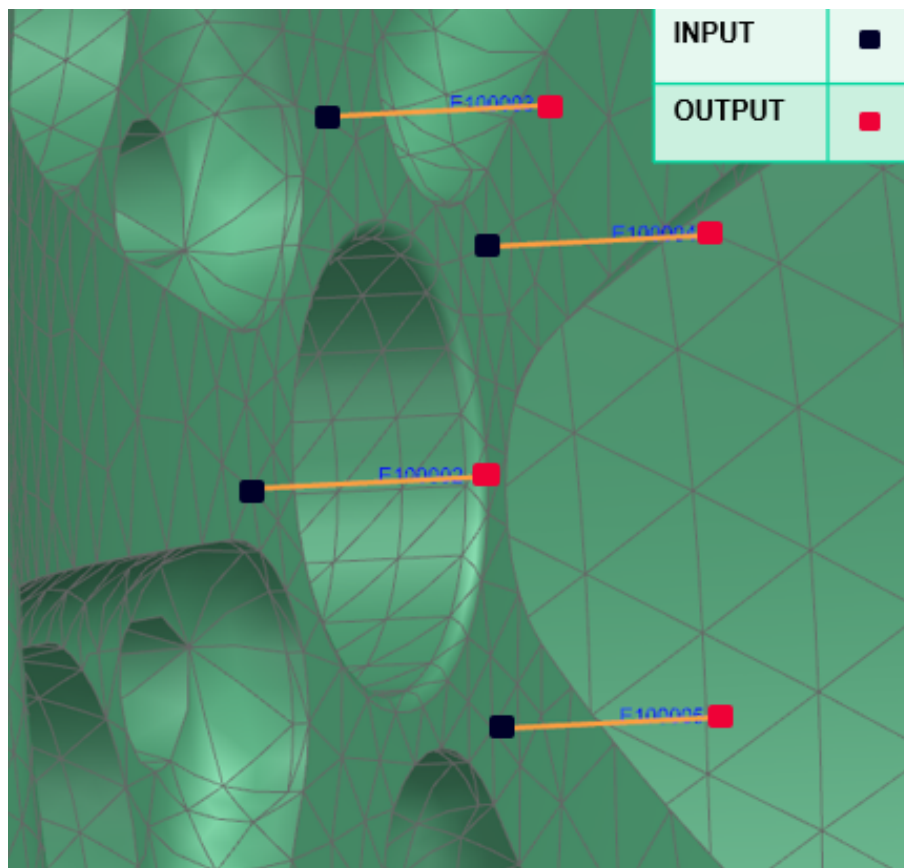


Figure 4.26: Second case reproducing sensors, input in the surface of contact and output on top.

The responses obtained show the same results of the previous case, namely the reciprocity plus the fact that this kind of discrepancy between the input and output locations does not affect the overall quality of the VPT, as it is showed in picture 4.27.

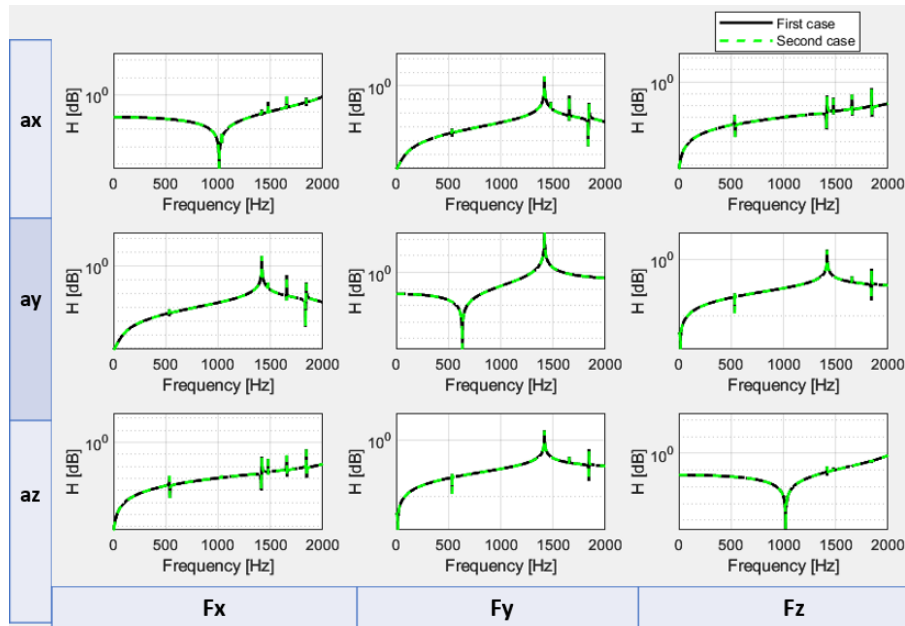


Figure 4.27: Comparison between the responses of the first and second case.

To summarize:

1. From the sensitivity analysis it is showed how the virtual point transformation method requires to rely on specific conditions such as the hypothesis of rigidity as well as to choose carefully the location of the indicators considering a region that can ensure a rigidity as much homogeneous as possible.
2. From the environmental error analysis it is highlighted the decrease on the accuracy of the method with possible errors in a real testing environment, focusing on the automotive rim. Specifically the error increase moving the indicators in regions subjected to more flexibility as the radius.
3. It is reported the dependency of the results quality from the relative location between the input shaker and the accelerometer sensor in different configurations.
4. Considering the input shaker and the output accelerometer as a unique rigid body, the responses measured with the VPT method are not influenced from the relative position between the input and the output.

Chapter 5

Modal analysis for Coupled Interfaces

In this chapter the aim is to analyze the various cases of couplings and how they affect the virtual point transformation method. Furthermore specific critical modes are investigated, firstly applying the virtual point transformation to detect them and then analyzing the animation of the modes leveraging the SOL103 (Real Eigenvalue Analysis). The model of the automotive rim and hub coupled is showed in figure 5.1.

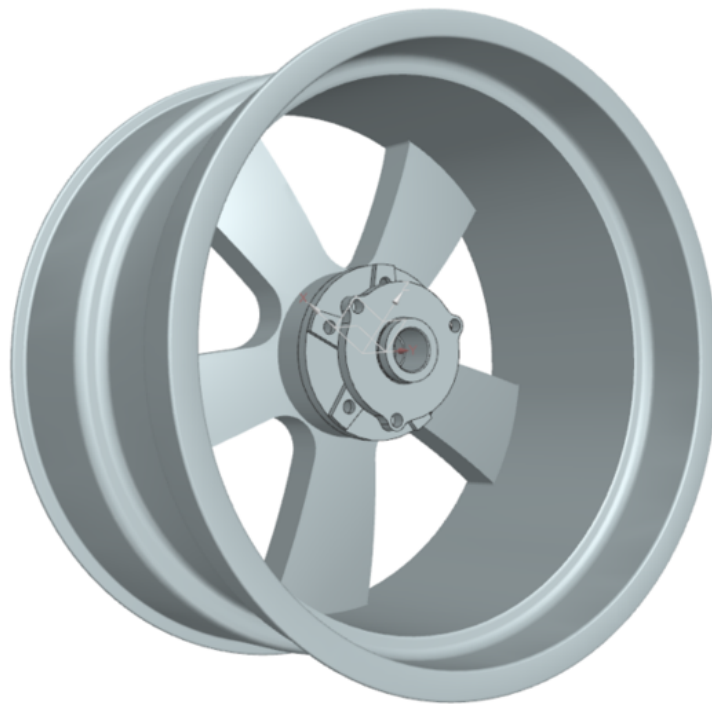


Figure 5.1: 3D model of the automotive rim and hub coupled.

The model of the automotive hub is designed from scratch taking inspiration from reliable models and seized to be coupled with the rim, as represented in figure 5.2.

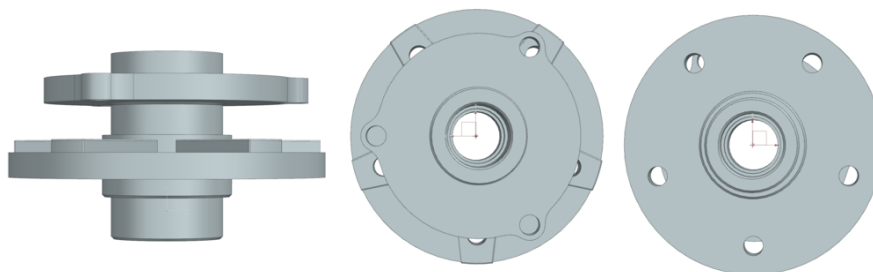


Figure 5.2: 3D model of the automotive hub.

Typically in a real physical environment the coupling is done through bolts, in this instance the two models are designed with five holes for this kind of connection in order to be a reliable representation of the real counterpart.

Assumptions:

- The material leveraged for all the cases of coupling in both the automotive rim and hub is the *Aluminum 6061* that shows good performances for this component [40]. The young modulus is $E = 6.898 \cdot 10^{10} Pa$, the volumetric density is $\rho = 2711 \frac{kg}{m^3}$ and the poisson's ratio is $\nu = 0.33$.
- The elements of the mesh implemented for the FEA are tetrahedral with 10 nodes each, the *Element size factor* = 0.5. The surface meshing method of *Mesh from facets* is also implemented in order to optimize automatically the size of the elements in narrow regions.
- For all the cases the selected virtual point lay on the $x - z$ plane at the same level of the plane that represents the surface of contact between the components, located on the center of the main hole. In order to fix this node physically to the structure a "spider" is implemented, that is a set of rigid connections leveraging the card *RBE2*. The rigid connections are between the virtual point and the edge of the main hole on the rim side from the surface of contact.
- For all the cases the analysis is done leveraging the solver *SOL111* in the range of frequencies from $0Hz$ to $8000Hz$ since the automotive hub shows the first mode at the frequency of $5372.5Hz$.

5.1 Glued connection

In this case the purpose is to obtain a connection that can reproduce the automotive rim and hub as a whole body. As a consequence this is the connection that presents the maximum rigidity. Considering the surface of contact between the two component, two regions are created on the software Simcenter 3D: one for the surface of contact of the rim and the other one for the hub surface. Then, always on the software Simcenter 3D, the command "*FaceGluing*" is leveraged. The results of the connection are showed in figure 5.3.

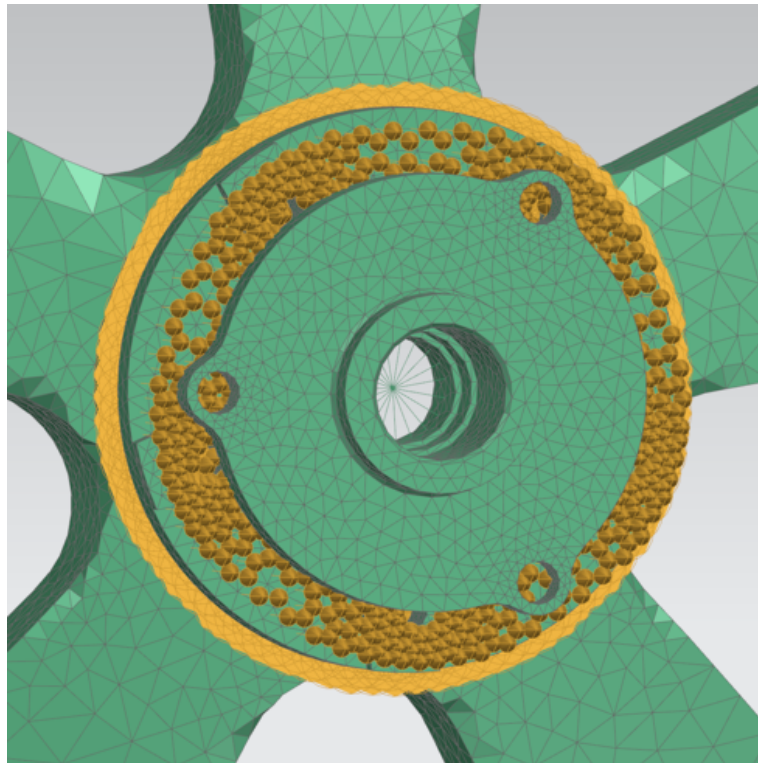


Figure 5.3: Focus on the connection on the "*Glued connection*" case.

The cards implemented with the utilisation of the "*Face Gluing*" command are **BGADD** [41], **BGSET** [42] and **BSURF** [43].

5.2 Single rigid connection

In this case a kind of connection that physically is not obtainable is implemented, the purpose is to retrieve an extreme case in which the rigidity should be the weakest among the other cases taken into account. The coupling is shown in figure 5.4.

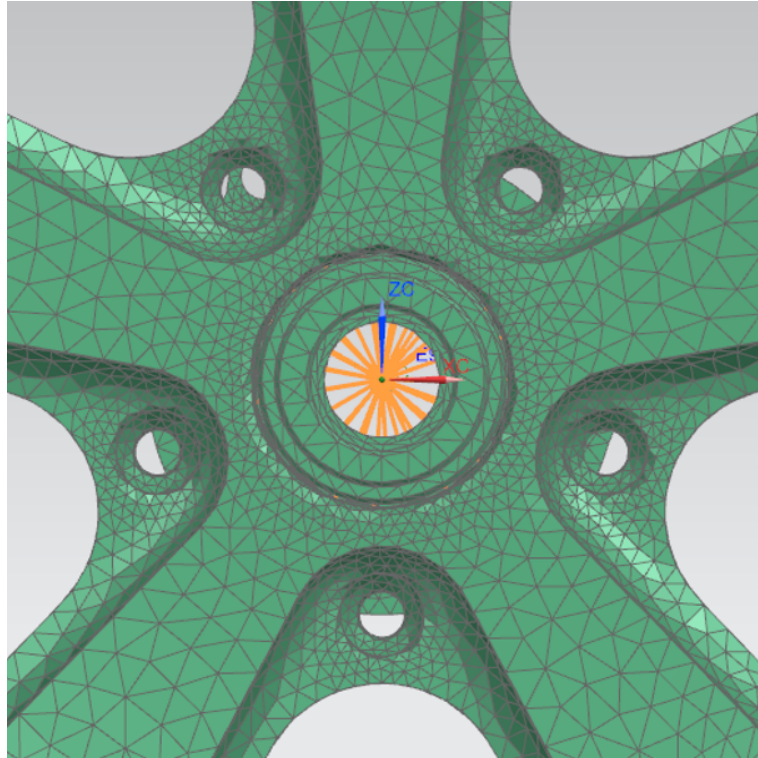


Figure 5.4: Focus on the connection on the "*Single rigid connection*" case.

One spider is leveraged for each component on the main hole connected to one node each on the same location of the virtual point, then through a single rigid connection the two centers of the spiders are connected.

5.3 Multiple rigid connection

The aim of this connection is to reproduce a connection with five bolts that the real physical connection. The connection is shown in figure 5.5.

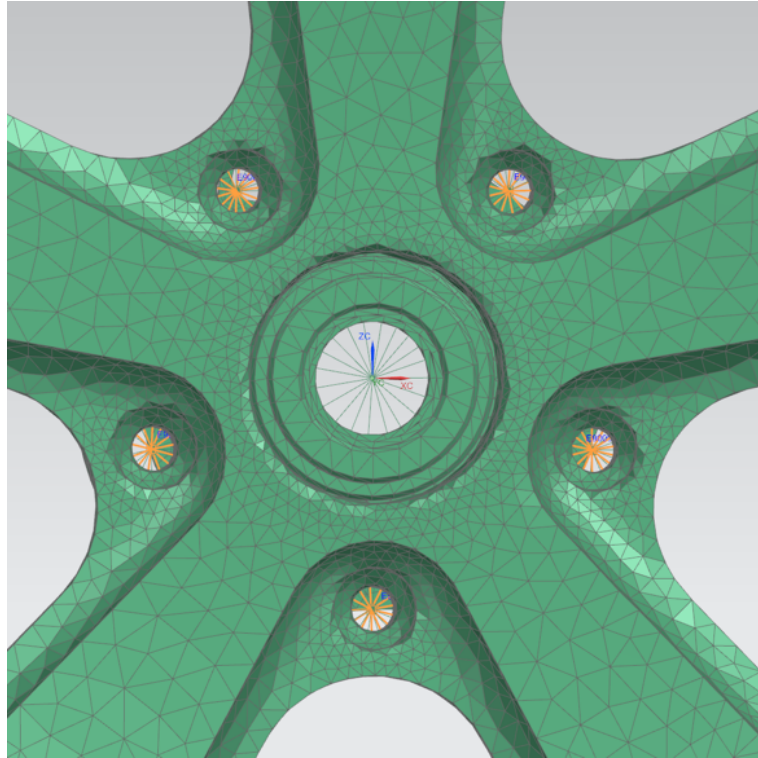


Figure 5.5: Focus on the connection on the "Multiple rigid connection" case.

In order to obtain this connection one pair of spiders is implemented for each hole: one spider fixed to the rim and one fixed to the hub. Then in each pair the centers of the two spiders are connected with one RBE2 card. In total there are five pairs of spiders, one for each hole.

5.4 Comparison & analysis

Hereafter the different rigidity ensuing from the different coupling is compared. The analysis is conducted leveraging the real eigenvalue analysis with the SOL103 in order to retrieve all the modes of the cases and the natural frequencies, then validate them computing the response with the SOL111 through the virtual point transformation method:

- A first hint on the different rigidity can be retrieved from the fact that until $8000Hz$ there is a different number of modes, namely the merged connection present the lower number of modes, whereas the connection with the higher number of modes is the single rigid connection, which as it can be expected should be the most flexible. The number of modes for the considered configurations is reported in table 5.1.

| | Modes under $8000Hz$ |
|----------|----------------------|
| Glued | 136 |
| Multiple | 138 |
| Single | 142 |

Table 5.1: Number of modes showed under $8000Hz$.

- The response applying the virtual point transformation method on the $y-axis$ is compared, considering as input F_y and as output a_y . The response is shown in figure 5.6.

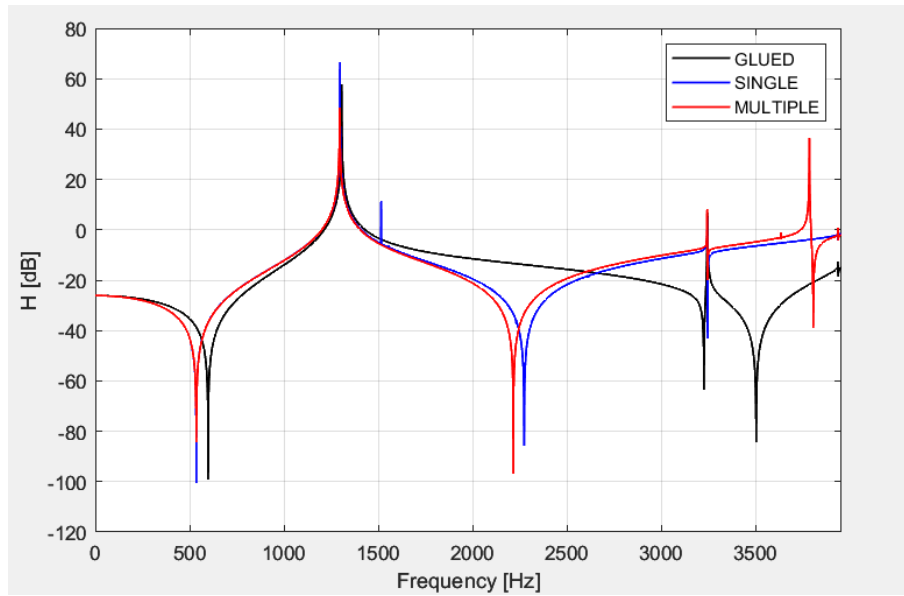


Figure 5.6: Comparison of the response with input F_y and output a_y : range of frequencies $0\text{Hz} - 4000\text{Hz}$.

The most significant mode that shows differences in rigidity is the 11 - *th* mode as showed in figure 5.7.

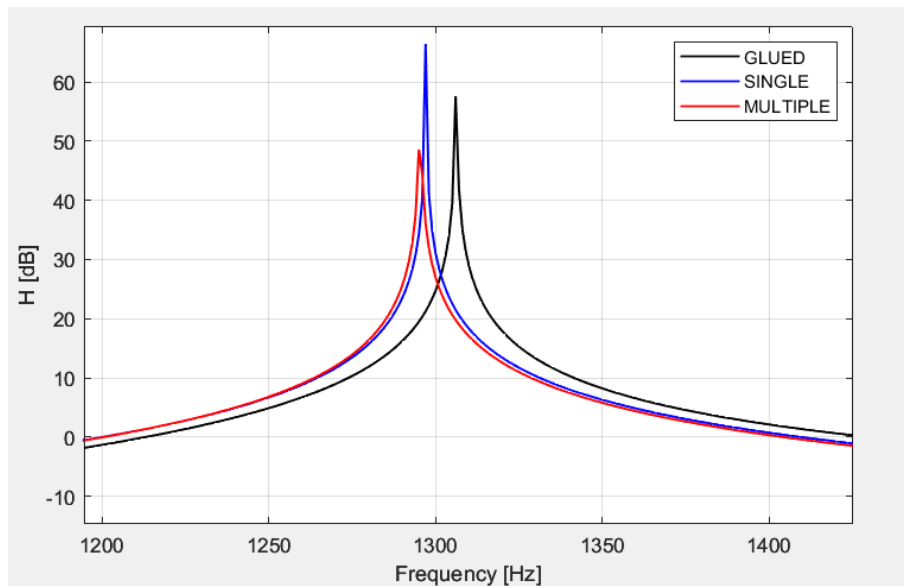


Figure 5.7: Mode 11 response with input F_y and output a_y .

From the plot of the response it can be noted that the mode for the glued connection is at higher frequency, that is $1305Hz$, due to its higher rigidity, whereas the modes of the multiple and single connection have a natural frequency respectively at $1295Hz$ and $1297Hz$. A further result is that the higher discrepancy between the glued connection from the others in terms of rigidity is reflected on the fact that the shape of the response is not following the single and multiple. The weaker connection of the single one is ensuing from the value of the mode shape that it considerably the greatest among the others. The deformation ensuing from the eleventh mode is shown in figure 5.8.

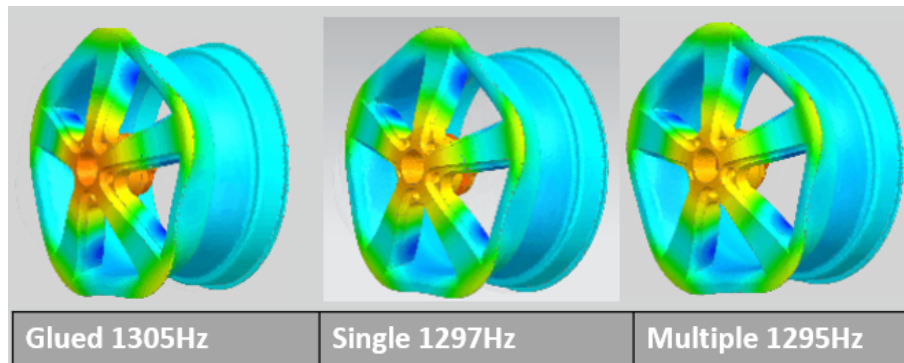


Figure 5.8: Mode 11 response with input F_y and output a_y , animations on Simcenter 3D.

- The greater instability of the single connection with respect to the other cases is showed on the plane $x - z$. In picture 5.9 the plot of the responses considering the input and the output along the $z - axis$ is represented.

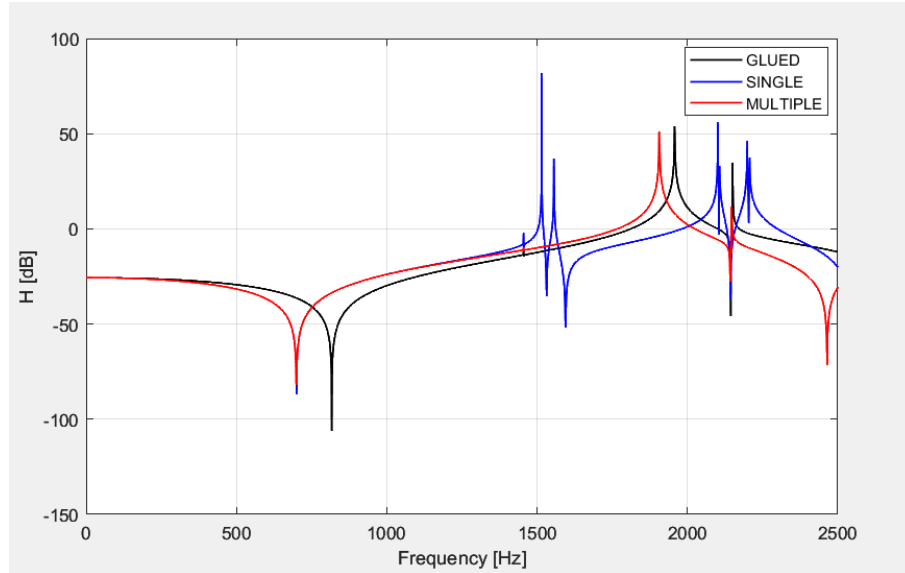


Figure 5.9: Comparison of the response with input F_z and output a_z : range of frequencies $0Hz - 2500Hz$.

It can be noted that the single connection after the mode at $1455Hz$ presents two modes immediately at $1515Hz$ and $1556Hz$ whereas the other ones remain stable until $1908Hz$. In figure 5.10 the significant modes on the response with input F_z and output a_z are highlighted.

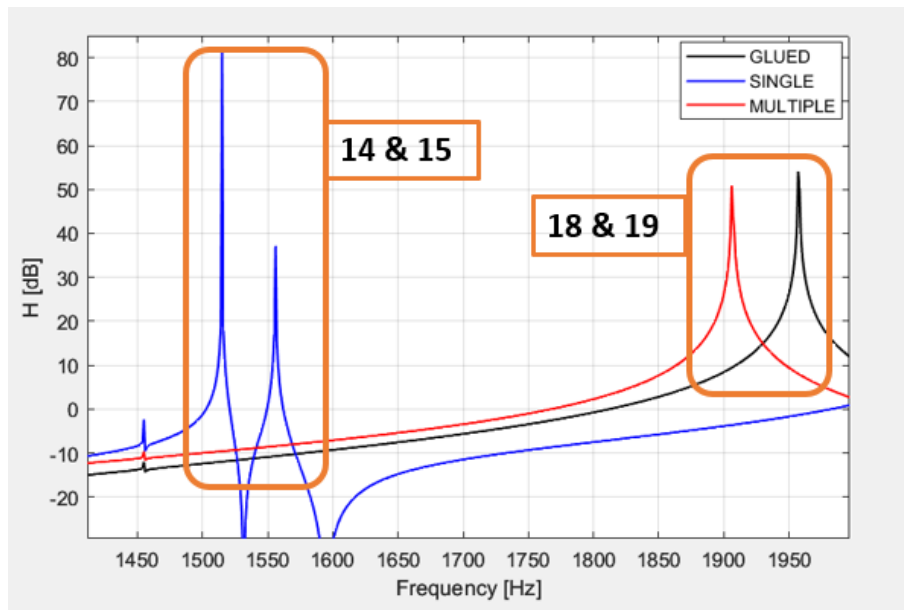


Figure 5.10: Significant modes, response with input F_z and output a_z .

The single rigid connection if solicited on the $x - z$ axis presents three modes in the range from $1450Hz$ to $1600Hz$, looking at the real eigenvalue analysis it can be noted that only this connection presents this weakness in this range, as shown in picture 5.11.

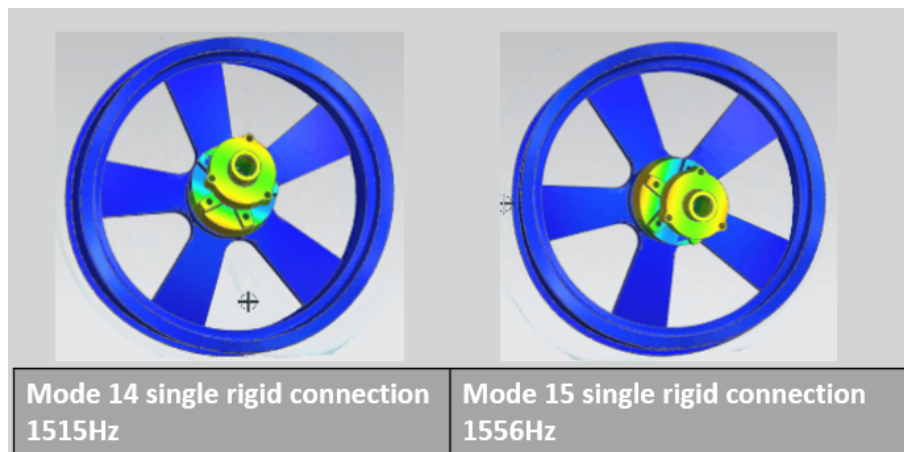


Figure 5.11: Modes 14 – *th* and 15 – *th* for the single rigid connection, input load F_z .

This can ensue from the lower rigidity of the connection between the hub and the rim that allows more freedom to move of the two components along the $x - z$ plane. On the other hand it can be seen from the real eigenvalue analysis that from the mode at the natural frequency of $1456Hz$ the next significant modes for the multiple and glued connections on the $x - z$ plane are hastened at higher frequencies compared to the single rigid connection this imply that they are more rigid on this plane. It is shown in picture 5.12 respectively the mode 18 – th for the multiple and the glued connections respectively at $1908Hz$ and $1958Hz$.



Figure 5.12: Mode 18 – th for the multiple and glued connections, input load F_z .

To summarize on the $x - z$ plane the single rigid connection is the weakest as it can be expected, furthermore it can be understood that the multiple rigid connection has better performance compared to it, which are more closer to the glued connection performances in terms of rigidity.

To summarize different considerations can be done:

- The virtual point transformation method relies on the hypothesis of rigidity, namely ideally there should be an ideal rigid connection between the virtual point and the indicators to obtain appreciable quality on the results. The rigidity can be obtained also ensuring that the indicators and the virtual point are located within an area with high rigidity. In this case the rigid connections between the virtual point and the indicators are not implemented in order to show that the quality of the method can be ensured also if the indicators and the virtual point are located in a region with great rigidity, and if it can substitute the rigid connections. The scale of the results perfectly reflects this dependency. The glued connection ensures the most wide area of rigidity ensuring the better stability and quality. Furthermore the single rigid

connection shows overall the worst results in term of stability and quality of the method applied, due to the narrowest region of rigidity, ensured only from the spider on the main center hole of connection.

- In order to implement the virtual point transformation method with the aim to gather a reliable behavior of the rim under real physical conditions, the user should chose a number of indicators equal to the holes that connect the hub and the rim. If the rim to be tested is that one considered in this analysis, the number of indicators should be equal to five. As a result from the analysis of this chapter, the indicators should be located close to the holes, namely the regions close to the points of connection should be that ones with the highest rigidity, leading to an appreciable accuracy of the method.
- In a testing environment, the set-up and the choice of the indicators to implement is left to the user. Choosing more indicators can be a solution that requires more economic efforts as well as in terms of time spent to chose the right location of the indicators and the time spent to analyze data from various sources. Even if choosing to use only one indicator can be a more simple and economic way, using more indicators such as five can lead to optimal quality of the results. Overall it is a tradeoff that has to be considered from the user between the quality of the method applied and the resources that this level of quality need to be obtained.

Chapter 6

Conclusions and further improvements

Through simulation, the modal analysis and the virtual point transformation method are demonstrated to be effective tools to analyze the performances of a component in the NVH field. The automotive wheel still represents one of the most complex systems to analyze and master due to its geometrical complexity. One of the biggest issues on implementing the virtual point transformation method on this kind of component is the flexibility of it that shows its effects at high frequencies, namely this is a relevant case of study for specialized professionals in the NVH field. The main purpose of this thesis project is to report an approach to the testing and validation phase of an automotive component, in particular leveraging CAE through one of the most effective simulation tools such as Simcenter Nastran and Simcenter 3D. What has been analyzed in this project is an attempt of the current engineering efforts to reproduce with CAE experimental errors of a real test bench. Before starting the real tests, retrieving through simulation the optimal configuration of the indicators can lead to a considerable decrease of the waste of time and money. Namely the accuracy of the VPT depend strongly on the correct geometrical data, represented by the distances between the indicators and the virtual point, and the quality of the FRFs acquired from the measurements. The optimization of this approach can represent a noticeable help for the professional figures in the testing phase. Future improvements are expected to come considering the virtual point transformation method and its contribute in Frequency-Based Dynamic Substructuring:

- One of the challenges of the virtual point transformation method is the reconstruction of the rotational response. The rotational response namely is that one that represents the most problems in terms of accuracy of the VPT. One method that is still on development has been reported in the paper

"Including directly measured rotations in the virtual point transformation" [33] in section 2.3.2. The formulation of the transformation matrices Ψ_f and Ψ_a can be expanded with data gathered from a triaxial rotation sensor. This method is under study, as a consequence it still need to be optimized.

- Another method of which the development is still ongoing is the multi-point virtual point transformation. This method is an extension of the VPT. Starting from the response retrieved in the virtual point, the response is then utilized as an indicator response reapplying the VPT to a further virtual point. Basically the indicators responses of the VPT are retrieved from previous virtual points responses.
- An optimal quality of the virtual point transformation method can represent a key-point for the implementation of the Frequency-Based Substructuring. This can allow the perfect accuracy of the FBS and open the doors to further uses of the FBS not only in the aerospace and automotive fields.

Bibliography

- [1] Enginesoft. *L'importanza dell'analisi dell NVH nello sviluppo di trasmissioni meccaniche*. Feb. 2020. URL: <https://newsroom.enginsoft.com/limportanza-dellanalisi-dellnvh-nello-sviluppo-di-trasmissioni-meccaniche> (cit. on p. 2).
- [2] Kistler Group. *NVH (noise, vibration, harshness)*. URL: <https://www.kistler.com/en/glossary/term/nvh-noise-vibration-harshness/> (cit. on p. 2).
- [3] Wang XU. *Vehicle noise and vibration refinement*. Cambridge, UK, 2010 (cit. on p. 3).
- [4] IPETRONIK. *NVH measurements on HVAC compressor systems*. URL: <https://www.ipetronik.com/en/industries/practical-examples/automotive/nvh-measurements-%20on-hvac-compressor-systems.html> (cit. on p. 3).
- [5] AVL. *Solution for NVH simulations of transmissions and drivelines*. URL: <https://www.avl.com/-/solution-for-nvh-simulations-of-transmissions-and-drivelines> (cit. on p. 3).
- [6] Hyundai motor. *NVH A Completely New Level of Sound Control*. URL: <https://tech.hyundaimotorgroup.com/essential-performance/nvh/> (cit. on p. 3).
- [7] DEWESoft. *Vehicle NVH Testing-Noise, Vibration, and Harshness*. URL: <https://dewesoft.com/applications/nvh-testing> (cit. on p. 4).
- [8] PCB PIEZOTRONICS. *Accelerometers and Vibration Sensors for Research Development*. URL: <https://www.pcb.com/sensors-for-test-measurement/accelerometers> (cit. on p. 4).
- [9] G. Rossi. *Misure meccaniche e termiche*. 2010 (cit. on p. 4).
- [10] GRAS Sound and Vibration. *Manual*. URL: <https://www.grasacoustics.com/component/dc/?> (cit. on pp. 4, 5).

-
- [11] Siemens PLM. *Siemens PLM products: Exciters*. URL: <https://www.plm.automation.siemens.com/global/it/products/simulation-test/exciters.html> (cit. on p. 5).
- [12] Young Hoon Kim Mario Paz. *Structural Dynamics: Theory and Computation*. 2018 (cit. on p. 6).
- [13] Maarten van der Seijs. «Experimental Dynamic Substructuring: Analysis and Design Strategies for Vehicle Development». PhD thesis. TU Delft (cit. on pp. 6, 7).
- [14] Dennis de Klerk and Sven N.Voormeren. «General Framework for Dynamic Substructuring: History, Review and Classification of Techniques». In: *AIAA Journal* (2008) (cit. on p. 7).
- [15] Siemens PLM. *Transfer Path Analysis*. URL: <https://www.plm.automation.siemens.com/global/en/products/simulation-%20test/component-based-transfer-path-analysis.html> (cit. on p. 8).
- [16] Siemens PLM. *FRF Based Substructuring*. URL: <https://community.sw.siemens.com/s/article/FRF-Based-Substructuring> (cit. on p. 8).
- [17] Current Automotive. *Electric Vehicle and Tesla Experts*. URL: <https://www.currentautomotive.com/the-past-present-and-future-of-electric-vehicle-%20transmissions/> (cit. on p. 9).
- [18] Gerd Marbjerg Lukke Møller Iversen and Hans Bendtsen. *Noise from electric vehicles - 'state of the art' literature survey*. Internoise congress. Sept. 2013 (cit. on pp. 9, 10).
- [19] Raja Ishak Raja I.Salleh M.Z.Md zain. *Evaluation of Annoyance and Suitability of a Back-Up Warning Sound for Electric Vehicles*. International Journal of Automotive and Mechanical Engineering. Dec. 2013 (cit. on pp. 10, 11).
- [20] P. Seshu. *Textbook of finite element analysis*. 2018 (cit. on pp. 14, 16).
- [21] Siemens PLM. *Modal Analysis*. URL: <https://www.plm.automation.siemens.com/global/en/our-story/glossary/modal-%20analysis/13172> (cit. on p. 18).
- [22] Brüel and Kjær. *Structural Testing*. URL: <https://www.bksv.com/media/doc/br0458.pdf> (cit. on p. 18).
- [23] AUTODESK Help. *Frequency Response Analysis*. URL: <https://knowledge.autodesk.com/support/inventor-nastran/learn-explore/caas/CloudHelp/%20cloudhelp/2018/ENU/NINCAD-SelfTraining/files/GUID-FCA4E4B5-1A53-480E-A43A-%20A208E8F3C97E-htm.html> (cit. on p. 20).
- [24] SIEMENS-Simcenter Nastran Basic Dynamic Analysis User's Guide. *Direct Frequency Response Analysis (SOL108)*. URL: https://docs.plm.automation.siemens.com/tdoc/nx/1899/nx_help/#uid:id471526 (cit. on p. 20).

- [25] SIEMENS-Simcenter Nastran Basic Dynamic Analysis User's Guide. *Modal Frequency Response Analysis (SOL111)*. URL: https://docs.plm.automation.siemens.com/tdoc/nx/1899/nx_help/#uid:id471531 (cit. on p. 20).
- [26] D. de klerk. «How Bias Errors Affect Experimental Dynamic Substructuring». In: *Proc. 28th International Modal Analysis Conference*. 2011, pp. 1101–1112 (cit. on p. 23).
- [27] S. N. Voormeeren D. de klerk. «Uncertainty Propagation in Experimental Dynamic Substructuring». In: *Proc. 26th International Modal Analysis Conference*. 2008 (cit. on p. 23).
- [28] S.W.B. Klaassen E. A. Pasma M. V. van der Seijs. «Frequency Based Substructuring with the Virtual Point Transformation». In: *Proc. of the Society for Experimental Mechanics Series 4*. 2018, pp. 205–213 (cit. on p. 23).
- [29] W. G. Flannely B. Jetmundsen R. L. Bielawa. «Generalized Frequency Domain Substructure Synthesis». In: *Journal of the American Helicopter Society* 33 (1988), pp. 55–64 (cit. on p. 24).
- [30] J. de Jong D. de Klerk D. J. Rixen. «The Frequency Based Substructuring (FBS) Method reformulated according to the Dual Domain Decomposition Method». In: *Proc. of the 24th International Modal Analysis Conference*. 2006 (cit. on p. 24).
- [31] M. van der Seijs et al. «An improved methodology for the virtual point transformation of measured frequency response functions in dynamic substructuring». In: *Proc. in 4th ECCOMAS Thematic Conference on Computational Methods in Structural Dynamics and Earthquake Engineering (COMPDYN)*. 2013, pp. 4334–4347 (cit. on p. 24).
- [32] E. A. Pasma et al. «Frequency Based Substructuring with the Virtual Point Transformation, Flexible Interface Modes and a Transmission Simulator». In: *Proc. of the Society for Experimental Mechanics Series 4*. 2018, pp. 205–213 (cit. on pp. 24, 29).
- [33] Daniel Rixen et al. «Including directly measured rotations in the virtual point transformation». In: *Mechanical Systems and Signal Processing* (Oct.2019) (cit. on p. 24).
- [34] D. de Klerk et al. «The Frequency Based Substructuring (FBS) Method reformulated according to the Dual Domain Decomposition Method». In: *Proc. of the 24th International Modal Analysis Conference*. 2006 (cit. on p. 24).

- [35] M. van der Seijs et al. «An improved methodology for the virtual point transformation of measured frequency response functions in dynamic substructuring». In: *Proc. in 4th ECCOMAS Thematic Conference on Computational Methods in Structural Dynamics and Earthquake Engineering (COMPdyn)*. 2013, pp. 4334–4347 (cit. on p. 24).
- [36] E. A. Pasma et al. «Frequency Based Substructuring with the Virtual Point Transformation, Flexible Interface Modes and a Transmission Simulator». In: *Proc. of the Society for Experimental Mechanics Series 4*. 2018, pp. 205–213 (cit. on p. 25).
- [37] A. Drozg et al. «On the performance of direct piezoelectric rotational accelerometers in experimental structural dynamics». In: 98 (2018), pp. 292–298 (cit. on p. 28).
- [38] D. J. Ewins. *Modal Testing: Theory and Practice*. Studies Press Ltd., 1984 (cit. on p. 28).
- [39] (CAE Analyst) Sourav Das. «Design and Weight Optimization of Aluminium Alloy Wheel». In: *International Journal of Scientific and Research Publications* 4.6 (2014) (cit. on p. 41).
- [40] Pune University Bhushan Mohite Mechanical Engineering Department. «Stress Analysis and Optimization of Front Wheel Hub». In: *IJRASET* 6 (2018) (cit. on p. 72).
- [41] SIEMENS-Simcenter Nastran Quick Reference Guide. *BGADD Surface-to-surface Glue Set Combination*. URL: https://docs.plm.automation.siemens.com/tdoc/nx/1899/nx_help/#uid:id569972 (cit. on p. 73).
- [42] SIEMENS-Simcenter Nastran Quick Reference Guide. *BGSET Glue Contact Set Definition*. URL: https://docs.plm.automation.siemens.com/tdoc/nx/1899/nx_help/#uid:id507351 (cit. on p. 73).
- [43] SIEMENS-Simcenter Nastran Quick Reference Guide. *BSURF Contact or Glue or Co-Simulation (Wetted) Region using Shell Elements*. URL: https://docs.plm.automation.siemens.com/tdoc/nx/1899/nx_help/#uid:id507356 (cit. on p. 73).